

GRB-SN Association within the Binary-Driven Hypernova Model

Y. AIMURATOV,^{1,2} L. M. BECERRA,^{3,2} C.L. BIANCO,^{2,4,5,6} C. CHERUBINI,^{2,7,8} M. DELLA VALLE,^{9,2} S. FILIPPI,^{2,7,10}
LIANG LI (李亮),^{2,4,11} R. MORADI,^{2,4,11} J. A. RUEDA,^{2,4,12,13,6} R. RUFFINI,^{2,4,5,14} N. SAHAKYAN,^{2,15} Y. WANG (王瑜),^{2,4,11}
AND S. R. ZHANG (张书瑞)^{2,12,13,16,17}

¹Fesenkov Astrophysical Institute, Observatory 23, 050020 Almaty, Kazakhstan

²International Center for Relativistic Astrophysics Network, Piazza della Repubblica 10, I-65122 Pescara, Italy

³Escuela de Física, Universidad Industrial de Santander, A.A.678, Bucaramanga, 680002, Colombia

⁴ICRA, Dipartimento di Fisica, Sapienza Università di Roma, Piazzale Aldo Moro 5, I-00185 Roma, Italy

⁵Université de Nice Sophia-Antipolis, Grand Château Parc Valrose, Nice, CEDEX 2, France

⁶INAF, Istituto di Astrofisica e Planetologia Spaziali, Via Fosso del Cavaliere 100, 00133 Rome, Italy

⁷ICRA, University Campus Bio-Medico of Rome, Via Alvaro del Portillo 21, I-00128 Rome, Italy

⁸Department of Science and Technology for Humans and the Environment and Nonlinear Physics and Mathematical Modeling Lab,
University Campus Bio-Medico of Rome, Via Alvaro del Portillo 21, 00128 Rome, Italy

⁹INAF - Osservatorio Astronomico di Capodimonte, Salita Moiariello 16, I-80131, Napoli, Italy

¹⁰Department of Engineering, University Campus Bio-Medico of Rome, Nonlinear Physics and Mathematical Modeling Lab,
Via Alvaro del Portillo 21, 00128 Rome, Italy

¹¹INAF, Osservatorio Astronomico d'Abruzzo, Via M. Maggini snc, I-64100, Teramo, Italy

¹²ICRANet-Ferrara, Dip. di Fisica e Scienze della Terra, Università degli Studi di Ferrara, Via Saragat 1, I-44122 Ferrara, Italy

¹³Dipartimento di Fisica e Scienze della Terra, Università degli Studi di Ferrara, Via Saragat 1, I-44122 Ferrara, Italy

¹⁴INAF, Viale del Parco Mellini 84, 00136 Rome, Italy

¹⁵ICRANet-Armenia, Marshall Baghramian Avenue 24a, Yerevan 0019, Republic of Armenia

¹⁶School of Astronomy and Space Science, University of Science and Technology of China, Hefei 230026, China

¹⁷CAS Key Laboratory for Research in Galaxies and Cosmology, Department of Astronomy, University of Science and Technology of China, Hefei 230026, China

(Dated: Received date / Accepted date)

Submitted to ApJ

ABSTRACT

The observations of Ic supernovae (Ic/SNe) occurring after the prompt emission of long gamma-ray bursts (GRBs) are addressed within the binary-driven hypernova (BdHN) model. The GRBs originate from a binary composed of a $\sim 10 M_{\odot}$ carbon-oxygen (CO) star and a companion neutron star (NS). We assume these same progenitors originate the Ic/SN. The binary evolution depends strongly on the binary period, P_{bin} . The trigger, given by the CO core collapse, for P_{bin} of up to a few hours leads to an Ic/SN with a fast-spinning NS (ν NS) at its center. For $P_{\text{bin}} \sim 4\text{--}5$ min, BdHN I occur with energies $10^{52}\text{--}10^{54}$ erg, a contribution by the black hole (BH) created by the NS companion collapse, originates the MeV/GeV radiations. The ~ 1 millisecond ν NS originates, by synchrotron radiation, the X-ray afterglow. For $P_{\text{bin}} \sim 10$ min, BdHN II occurs with energies of $10^{50}\text{--}10^{52}$ erg. For $P_{\text{bin}} \sim$ hours, BdHN III occurs with energies below 10^{50} erg. The 1–1000 ms ν NS, in all BdHNe, originates the X-ray afterglow by synchrotron emission. The SN Ic follows an independent evolution, becoming observable by the nickel decay after the GRB prompt emission. We report 24 Ic/SNe associated with BdHNe; their optical peak luminosity and their time of occurrence are similar and independent of the associated GRBs. We give four examples of BdHNe and their associated hypernovae. For the first time, we approach new physical processes in BdHNe, identifying seven episodes and their signatures in their spectra.

Keywords: gamma-ray bursts: general — optical: general — stars: neutron — supernovae: general — black hole physics

1. INTRODUCTION

Since their discovery, the enormous energetics led to the idea that GRBs are associated with massive stars' gravitational collapse, leading to neutron stars (NSs) or black holes (BHs). The community widely accepts the seminal proposal that mergers of NS-NS or NS-BH binaries are the progenitors of short GRBs (Goodman 1986; Paczynski 1986; Eichler, David et al. 1989; Narayan et al. 1991). For long GRBs, our sources of interest here, the traditional model is based on a *collapsar*, the core-collapse of a single massive star leading to a BH (or a magnetar) surrounded by an accretion disk (Woosley 1993). We refer the reader to Mészáros (2002); Piran (2004), for comprehensive reviews.

In the GRB traditional model, the prompt emission originates in the dynamics, expansion, and transparency of a *fireball*, an optically thick electron-positron (e^-e^+)-photon plasma in equilibrium with baryons (Cavallo & Rees 1978; Paczynski 1986; Goodman 1986; Narayan et al. 1991, 1992). The fireball expands in a collimated relativistic jet with Lorentz factor $\Gamma \sim 10^2\text{--}10^3$ (Shemi & Piran 1990; Rees & Meszaros 1992; Piran et al. 1993; Meszaros et al. 1993; Mao & Yi 1994). In this picture, the interaction of internal and external shocks with the surrounding and interstellar medium are responsible for the prompt emission and the afterglow, including the very-high-energy (VHE) emission by synchrotron self-Compton radiation (Mészáros 2002; Piran 2004; MAGIC Collaboration et al. 2019; Zhang 2019). We refer to Zhang (2018) for the latest developments of the GRB traditional model.

From the energetics, dynamics, and radiation efficiency, two difficulties arise in the traditional model. 1) Only a small fraction of the energy of the ultra-relativistic jet is radiated by the synchrotron emission, so much of the kinetic energy remains in the jet. 2) The radiation from the jet implies the absence of afterglow in some long GRBs, while it is clear that the afterglow is present in all GRBs.

We now turn to one of this article's main topics, the GRB-SN connection. The follow-up of the optical afterglow, extended by the Neil Gehrels Swift Observatory (Barthelmy et al. 2005; Burrows et al. 2005; Roming et al. 2005), led to the discovery of the association of long GRBs with type Ic supernovae (SNe), first marked with the temporal and spatial coincidence of GRB 980425 and SN 1998bw (Galama et al. 1998). Since then, further observations have confirmed the GRB-SN connec-

tion (Woosley & Bloom 2006; Della Valle 2011; Hjorth & Bloom 2012). The association of GRBs with SNe Ic is possibly one of the most relevant observational clues for theoretical models. Several theoretical and observational consequences from the GRB-SN connection constrain models of GRBs and the associated SNe Ic:

(i) *Long GRBs and SNe have different energetics.* SNe radiate energies $\sim 10^{49}\text{--}10^{51}$ erg, while GRBs show energies in the much wider range $\sim 10^{49}\text{--}10^{54}$ erg. The energy release of energetic GRBs is associated with the gravitational collapse to a BH, while SNe originate in the core-collapse of a massive star to an NS.

(ii) *Most (if not all) long-duration GRBs originate from binary stars.* a) In recent decades, growing evidence has shown that long-duration GRBs are associated with the explosions of massive stars. This fact has been well established both on a statistical basis, e.g., Fruchter et al. (2006); Raskin et al. (2008); Kelly et al. (2008), and from stellar evolution which, even if constraining the zero-age main-sequence (ZAMS) mass of the SN progenitor is highly model-dependent, points undoubtedly to massive stellar progenitors from the modeling of the photometric and spectroscopic follow-up of SNe-Ibc associated with GRBs, e.g., SN 1998bw, $25\text{--}40M_\odot$ (Woosley & Bloom 2006; Maeda et al. 2006); SN 2003dh $35\text{--}40M_\odot$ (Nomoto et al. 2003; Mazzali et al. 2003); SN 2003lw $25M_\odot$ (Mazzali et al. 2006); 2008D $30M_\odot$ (Tanaka et al. 2009); 2010bh $25M_\odot$ (Bufano et al. 2012); 2016jca $35M_\odot$ (Ashall et al. 2019). b) It is well known that a significant fraction of massive stars are in binaries (about 70%, e.g., Kobulnicky & Fryer 2007 and Sana et al. 2012). c) In addition, although stellar evolution models predict the direct formation of a BH from the gravitational collapse for progenitor stars $\gtrsim 25M_\odot$ (Heger et al. 2003), two observational facts pose serious challenges to GRB-SN models in which both a BH and SN originate from a single-star: 1) the direct gravitational collapse of a massive star to a BH should occur without an SN emission; 2) observed pre-SN progenitors have masses $\lesssim 18 M_\odot$ (see Smartt 2009, 2015, for details). Therefore, it is unlikely that the GRB and the SN can originate from the very same single star. Indeed, it is an extreme request for the gravitational collapse of a massive star to form a collapsar, a jetted fireball, and an SN explosion. Some models attempt to supply (partial) solutions to these issues, like an efficient neutrino emission from the accretion disk (e.g. MacFadyen & Woosley 1999) or the presence of an outflow/wind

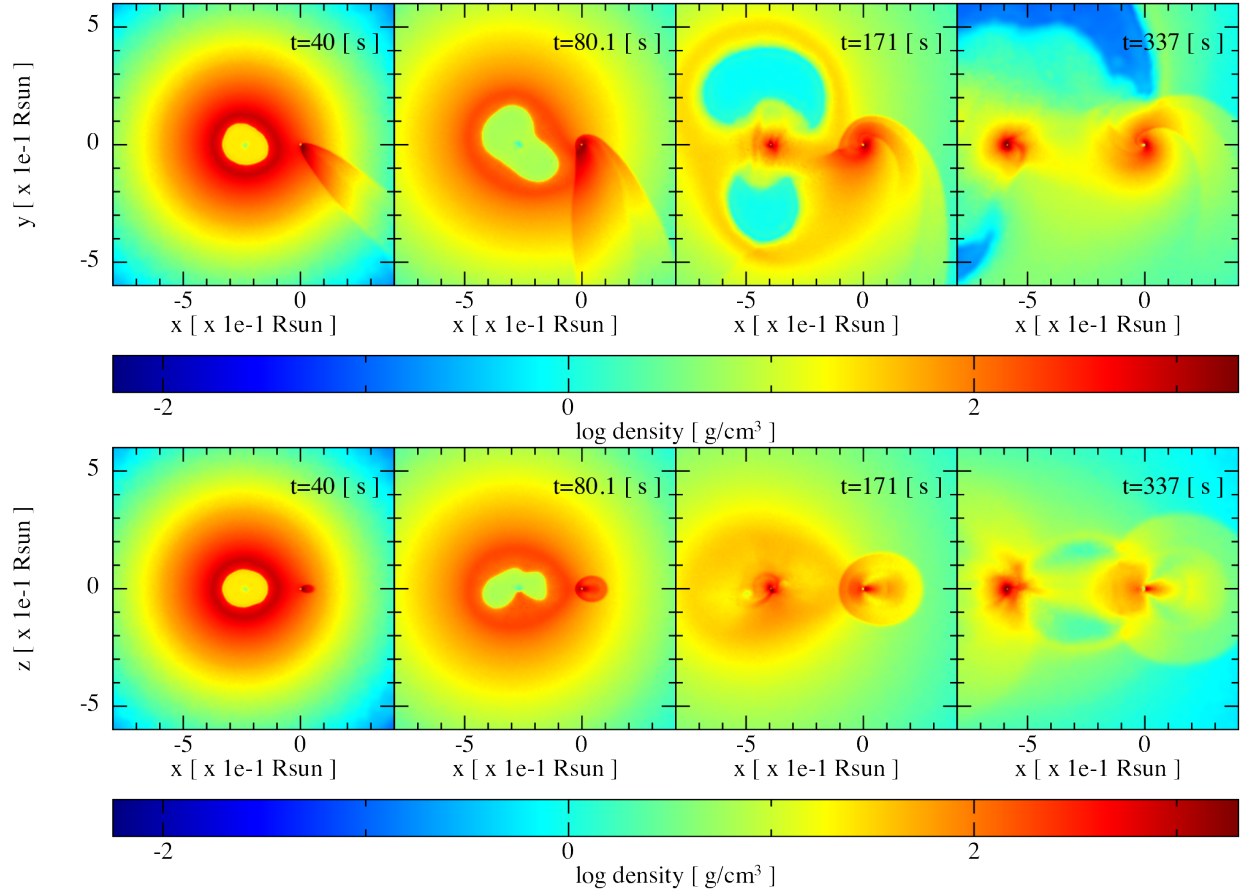


Figure 1. SPH simulation of a BdHN I: model “30m1p1eb” of Table 2 in [Becerra et al. \(2019\)](#). The binary progenitor comprises a CO star of $\approx 9M_{\odot}$ (produced by a ZAMS star of $30M_{\odot}$) and a $2M_{\odot}$ NS companion. The orbital period is ≈ 6 min. From left to right, each snapshot corresponds to selected increasing times where $t = 0$ s refers to the SN shock breakout. The upper and lower panel shows the mass density on the equatorial plane and in the plane orthogonal to the latter. The reference system is rotated and translated to align the x-axis with the line joining the binary components. The origin of the reference system is located at the NS companion position. In the first snapshot at $t = 40$ s, particles in the NS gravitational capture region form a tail behind the NS companion. These particles then circularize around the NS, forming a thick disk visible in the second snapshot at $t = 80$ s. Part of the ejecta produces a fallback accretion process onto the ν NS visible in the third snapshot at $t = 171$ s. At $t = 337$ s (about one orbital period), a disk structure is visible around the ν NS and the NS companion. This figure has been produced with the SNe splash visualization program ([Price 2011](#)).

where the nucleosynthesis of the nickel for the optical SN can occur (see, e.g., [Kohri et al. 2005](#); [Milosavljević et al. 2012](#); [Lindner et al. 2012](#)). The direct conclusion we can draw from the abovementioned points is that most long-duration GRBs occur in binaries. These facts motivated our development of a model for long-duration GRBs that fully exploit the binary nature of progenitors.

(iii) *The SNe associated with GRBs are of type Ic.* The lack of hydrogen (H) and helium (He) in the spectra of type Ic SNe has the leading explanation that they originate in bare He, carbon-oxygen (CO), or Wolf-Rayet (WR) stars that lose the outermost hydrogen and helium layers during their evolution (see, e.g., [Smith et al. 2011](#); [Teffs et al. 2020](#)). Numerical simulations indicate that the most natural mechanism for He/CO/WR stars to get rid of their H/He envelope is from in-

teractions with a compact-star companion (e.g., NS) through multiple mass-transfer and common-envelope phases (see, e.g., [Nomoto & Hashimoto 1988](#); [Iwamoto et al. 1994](#); [Fryer et al. 2007](#); [Yoon et al. 2010](#); [Smith et al. 2011](#); [Yoon 2015](#); [Kim et al. 2015](#)).

Although the above is not a complete list of possible drawbacks of the single-star scenario, it is already clear that considering alternatives is natural. In their pioneering work, [Fryer et al. \(1999\)](#) show that various binary stellar evolution channels can lead to diverse GRB events. This alternative binary approach has contributed, as mentioned above, in the study of short GRBs (see, e.g., [Ruffini et al. 2016a](#); [Aimuraton et al. 2017](#)), as well as an enigmatic long-lasting GRB without SN ([Della Valle et al. 2006a](#)) interpreted as a white dwarf (WD)-NS merger ([Caito et al. 2009](#); [Rueda et al. 2018](#)).

and the weakest GRBs from WD-WD mergers (see, e.g., Rueda et al. 2019b, 2022b).

We here specialize in the binary-driven hypernova (BdHN) model of long GRBs, which is based on the induced gravitational collapse (IGC) scenario (Rueda & Ruffini 2012). Following the evolution of stripped-envelope binaries, the BdHN model proposes as GRB progenitor a CO-NS binary at the end of the thermonuclear life of the CO star, i.e., the second core-collapse SN event in the binary lifetime. The first SN formed the NS companion of the CO star. The CO nature of the exploding star explains why the SN associated with the GRB is of type Ic, whereas the sequence of physical processes that the SN explosion triggers in the binary explains the seven episodes observed in the GRB (Rueda & Ruffini 2012; Izzo et al. 2012; Fryer et al. 2014, 2015; Becerra et al. 2015, 2016, 2019). Figure 1 shows an example of numerical simulation performed by Becerra et al. (2019) of the explosion of a CO star leading to a newborn NS (ν NS) and the SN Ic, in the presence of an NS companion. These simulations, which include hydrodynamics, neutrino emission, and general relativistic effects, show a variety of outcomes of the system, leading to a variety of GRB events, a BdHN classification, which we discuss below. One of the most relevant results is that, among the possible fates, the NS companion can reach the point of gravitational collapse, forming a rotating, newborn Kerr BH.

In Section 2, we recall the basics of the BdHN model and address how the interplay between the SN, ν NS, and NS companion leads to the variety of long GRBs.

Section 3 recalls a relativistic formulation’s framework in the source’s cosmological rest frame, including the k -correction.

In Section 4, we analyze 24 SNe associated with GRBs. We show that the SN bolometric peak luminosity and its time of occurrence in the source cosmological rest-frame are nearly the same for all sources (see Figs. 2 and 3). We also present the prompt gamma-ray energy (E_{iso}) of the associated GRB. We show that E_{iso} spans over six orders of magnitude, while the SN bolometric peak luminosity and the time of occurrence of the peak remain relatively constant; see Figs. 4 and 5. These results constrain GRB models and will be explained within the BdHN model in the following sections.

Section 5 describes the physical phenomena in the different BdHN types and relates them to specific GRB observables, namely the seven episodes of BdHNe; see Table 2 for details.

In Section 6, after recalling all the observations which have made possible the identification of this source as

BdHN I (Ruffini et al. 2018b), we address the seven episodes characterizing the GRB 180720B as a BdHN I.

Section 7 investigates the second BdHN I fully understood in the BdHN model: GRB 190114C (Ruffini et al. 2021; Moradi et al. 2021c). We recall the observations that identified this source as BdHN I (Ruffini et al. 2019b) and discuss its corresponding seven episodes, following an analogous presentation for GRB 180720B in Section 6.

In Section 8, we turn to the case of a BdHN II, GRB 190829A.

Since in BdHN II, the BH is not formed, the number of episodes in this GRB reduces from seven to three, which we address in detail.

In Section 9, we analyze the only example analyzed to date of a BdHN III: GRB 1711205A. Similar to BdHN II, in BdHN III, the BH is not formed.

The number of episodes in this GRB reduces from seven to two, which we present in detail.

Section 10 summarizes new physical phenomena triggered by the SN occurrence in BdHNe, not previously studied in the GRB physics literature.

Finally, we outline conclusions in Section 11.

2. BDHN CLASSIFICATION

The BdHN model assumes that some long GRB progenitors are binaries composed of a CO star of mass of $\sim 10M_{\odot}$ and a companion NS of $\sim 2.0M_{\odot}$. It also assumes that the gravitational collapse of the CO star generates an SN explosion and creates a newborn NS (ν NS) at its center. The ν NS with a mass of $1.5M_{\odot}$ is assumed to spin with a period of $\sim 1\text{--}100$ ms. It further assumes that $\sim 7\text{--}8M_{\odot}$ are ejected during the SN explosion. The theoretical motivations and the observation constraints leading to these assumptions are given in Sections 5–10, and implications are presented in the Conclusions (Section 11). The SN ejecta drives an accretion process onto the NS companion and a fallback accretion onto the ν NS. The accretion rates proceed at hypercritical rates (i.e., highly super-Eddington) due to the efficient neutrino emission (Fryer et al. 2014; Becerra et al. 2016, 2018). We differentiate three types of BdHN: I, II, and III, as a function of their overall energetics. A dependence of these energetics from the total initial angular momentum of the Co star-NS binary is evidenced. The shorter the binary period, the higher the BdHN total radiated energy.

2.1. BdHN I

We indicate by BdHN I the most energetic class of long GRBs with energies in the range of $10^{52}\text{ erg} \lesssim E_{\text{iso}} \lesssim 10^{54}\text{ erg}$. Their orbital period is of the order of $\gtrsim 5$ min,

which implies an orbital separation of $\sim 10^{10}$ cm, just bigger than the CO star radii (see, e.g., Fryer et al. 2014; Becerra et al. 2016, 2019). The hypercritical accretion of the SN ejecta onto the companion NS leads it to reach the critical mass, consequently forming a Kerr BH. Simulations show that the peak accretion rate onto the NS companion can reach $\dot{M}_{\text{peak}} \sim 10^{-3}\text{--}10^{-2}M_{\odot}\text{ s}^{-1}$, which implies accreting $0.5\text{--}1M_{\odot}$ in about one orbital period time (Becerra et al. 2016, 2019). The NS gains a large angular momentum, $\Delta J \sim GM_{\text{NS}}\Delta M_{\text{acc}}/c \sim 10^{49}$ g cm² s⁻¹, hence it reaches the critical mass at millisecond rotation rates. The accretion energy gain when bringing the NS to the critical mass and the energy involved in the BH formation process set a lower edge of $\sim 10^{52}$ erg of energy released in a BdHN I. Therefore, BdHN I explain the long GRBs with energies $E_{\text{iso}} \gtrsim 10^{52}$ erg (see Ruffini et al. 2018c, for details). The fallback accretion onto the ν NS also proceeds at hypercritical rates, and the presence of the NS companion generates a double-peak accretion (Becerra et al. 2019; see also Becerra et al. 2022 for recent simulations and implications). The first peak of accretion is of a few $10^{-3}M_{\odot}\text{ s}^{-1}$ and lasts for about one-tenth of the orbit (Becerra et al. 2019). The ν NS reaches a high rotation period of 0.5 ms, near the mass-shedding limit (Cipolletta et al. 2015). The fast-spinning ν NS gives origin to the GRB afterglow as explained in Section 5. Examples of BdHN I are GRB 180720B (see Section 6), GRB 190114C (Section 7), and GRB 130427A (Ruffini et al. 2019c, 2021).

Recently, a comprehensive analysis by Ruffini et al. (2021) of the long GRBs population with known redshift has led to the identification of 380 long GRBs as BdHN I, all endowed with an X-ray afterglow. The observed density rate of BdHN I is $\sim 1\text{ Gpc}^{-3}\text{ yr}^{-1}$ (Ruffini et al. 2016b, 2018c), which is consistent with GRB rates derived with different approaches (e.g., Guetta & Della Valle 2007). Therefore, a sub-population of $\approx 0.01\%\text{--}0.1\%$ ultra-stripped binaries is sufficient to explain the BdHN I population (see Fryer et al. 2015; Ruffini et al. 2016b, for details), given that ultra-stripped binaries comprise $0.1\%\text{--}1\%$ of the total SNe (see, e.g., Tauris et al. 2015); see also Section 11.

2.2. BdHN II

These binaries are characterized by longer orbital periods in the range of 20–40 min, so binary separations of a few 10^{10} cm. Numerical simulations show that in these binaries, the accretion rate onto the NS companion occurs at lower rates, $\dot{M}_{\text{peak}} \sim 10^{-5}\text{--}10^{-4}M_{\odot}\text{ s}^{-1}$. The NS does not reach the critical mass in these systems, so it does not form a BH. The above range of accretion rates implies that the BdHN II subclass can

explain long GRBs with energies $E_{\text{iso}} \sim 10^{50}\text{--}10^{52}$ erg (see, e.g., Ruffini et al. 2016b, 2018c).

Regarding the ν NS, although the first peak of fallback accretion is similar to that of BdHN I, the second peak is considerably lower, so in the end, the fallback accretion leads the ν NS to a slower rotation than its BdHN I counterpart. Still, the ν NS in BdHN II reaches rotation periods of a ~ 10 ms, sufficient to explain the afterglow by the associated synchrotron radiation; see Section 5. Examples of BdHN II are GRB 180728A (Wang et al. 2019) and GRB 190829A; see Section 8.

2.3. BdHN III

There are CO-NS binaries with orbital periods that can be even hours, corresponding to the binary separation of the order of a few 10^{11} cm. The accretion rate onto the NS companion is negligible, and the SN explosion likely disrupts the binary. In these cases, the fallback accretion onto the ν NS and its interaction with the SN ejecta are the only ones responsible for the long GRB emission. This BdHN III system explains low-luminous GRBs with an energy release of $E_{\text{iso}} \sim 10^{49}\text{--}10^{50}$ erg, and the ν NS reaches the period of $\sim 50\text{--}100$ ms, which are sufficient to explain the afterglow by the associated synchrotron emission; see Section 5. An example of BdHN III is GRB 171205A, for which we refer the reader to the recent and detailed analysis and simulations presented in Wang et al. (2022b) and Section 9.

From all the above, all BdHN types are endowed with an X-ray afterglow, which can be explained by the synchrotron radiation originating from the fast-spinning ν NS.

We now turn to the observational data of 24 long GRBs and associated Ic SNe and proceed to a selected sample of two BdHN I, one BdHN II, and one BdHN III and their associated HNe.

3. COSMOLOGICAL REST-FRAME TIME AND K -CORRECTION

We here introduce the conversion factor adopted in deriving a luminosity and time both in the cosmological rest-frame of the source (see Ruffini et al. 2018e). This conversion, known as k -correction, has been often neglected in the literature (Chincarini et al. 2007; Falcone et al. 2007; Margutti et al. 2010).

The observation time (t_{obs}) of the source is related to the time measured in the cosmological rest-frame (t_{rf}) on the earth by $t_{\text{obs}} = (1+z)t_{\text{rf}}$. The observed flux f_{obs} , namely the energy per unit area and time in a fixed detector energy bandwidth $[\epsilon_{\text{obs},1}; \epsilon_{\text{obs},2}]$, is

$$f_{\text{obs},[\epsilon_{\text{obs},1}; \epsilon_{\text{obs},2}]} = \int_{\epsilon_{\text{obs},1}}^{\epsilon_{\text{obs},2}} \epsilon n_{\text{obs}}(\epsilon) d\epsilon, \quad (1)$$

Table 1. GRB-SN spectroscopically confirmed sample

				This Study			Literature			
GRB	SN	SN	z	$E_{\text{iso},\gamma}$	$L_{\text{p,SN}}$	$t_{\text{p,SN}}$	$E_{\text{iso},\gamma}$	$L_{\text{p,SN}}$	$t_{\text{p,SN}}$	Data source
Name	Name	Type	Redshift	(erg)	($\times 10^{42}$ erg/s)	(days)	($\times 10^{52}$ erg)	($\times 10^{42}$ erg/s)	($\times 10^6$ s)	References
980425	1998bw	Ic-BL	0.0085	$(8.6 \pm 0.2) \times 10^{47}$	7.33	15.16	0.000086	14.5	1.30464	(1)–(5)
011121	2001ke	Ic	0.362	$(7.8 \pm 2.1) \times 10^{52}$	5.90	17	7.8	$\sim 5.9, 13.7$	1.4688	(3), (6)
021211	2002lt	Ic	1.006	$(1.12 \pm 0.13) \times 10^{52}$	7.20	14.00	0.828	—	2.16	(3), (7)–(11)
030329	2003dh	Ic	0.1687	$(1.5 \pm 0.3) \times 10^{52}$	10.1	12.75	1.515	10.1	1.1016	(3), (7)
031203	2003lw	Ic	0.1055	$(8.6 \pm 4.0) \times 10^{49}$	12.6	17.33	0.0098	12.6	1.497312	(3), (7)
050525	2005nc	Ic	0.606	$(2.5 \pm 0.43) \times 10^{52}$	4.47	13.10	2.945	—	—	(3), (12)
060218	2006aj	Ic-BL	0.0334	$(5.3 \pm 0.3) \times 10^{49}$	6.47	10.42	0.0053	6.47	0.90029	(3)
081007A	2008hw	Ic	0.5295	$(1.5 \pm 0.4) \times 10^{51}$	14.0	12.00	0.15	~ 14	~ 1.0368	(3)
091127	2009nz	Ic	0.4904	$(1.5 \pm 0.2) \times 10^{52}$	12.0	15.00	1.5	~ 12	~ 1.296	(3)
100316D	2010bh	Ic-BL	0.0592	$> 5.9 \times 10^{49}$	5.67	8.76	> 0.0059	5.67	0.756864	(3)
101219B	2010ma	Ic	0.5519	$(4.2 \pm 0.5) \times 10^{51}$	15.0	11.80	0.42	15	1.01952	(3)
111209A	2011kl	SLSN-I	0.677	$(5.82 \pm 0.73) \times 10^{53}$	29.1	14.80	58.2	29.1	1.27872	(3)
120422A	2012bz	Ib/c	0.2825	$(2.4 \pm 0.8) \times 10^{50}$	14.8	14.45	0.024	14.8	1.24848	(3)
120714B	2012eb	Ib/c	0.3984	$(5.94 \pm 1.95) \times 10^{50}$	6.20	13.60	0.3174195	—	13.6 ± 0.7	(3), (13)
130215A	2013ez	Ic	0.597	—	—	—	3.1	—	—	(3)
130427A	2013cq	Ic	0.3399	$(8.1 \pm 0.8) \times 10^{53}$	9.12	12.68	89	—	—	(3), (14)–(17)
130702A	2013dx	Ic-BL	0.145	$(6.4 \pm 1.3) \times 10^{50}$	10.8	12.94	0.064	10.8, 19.2	1.118016	(3), (6)
130831A	2013fu	Ib/c	0.4791	$(4.6 \pm 0.2) \times 10^{51}$	6.90	11.90	0.59221795	—	1.60704 ± 0.05789	(3), (13), (18)
161219B	2016jca	Ic-BL	0.1475	$(8.50 \pm 8.46) \times 10^{49}$	4.90	10.70	0.0858	10.4	0.92448	(6), (19), (20)
171010A	2017hfp	Ic-BL	0.33	$(1.80 \pm 0.30) \times 10^{53}$	8.4	12.80	18, 22	21 ± 9	—	(21)–(23)
171205A	2017iuk	Ic-BL	0.0368	$(5.72 \pm 0.80) \times 10^{49}$	6.5	15.08	0.00218	—	1.09728	(24)
180728A	2018fp	Ic-BL	0.117	$(2.30 \pm 0.10) \times 10^{51}$	5.8	12.70	0.2545	—	1.27008 ± 0.25056	(25)–(27)
190114C	2019jrj	Ic	0.4245	$(3.0 \pm 0.5) \times 10^{53}$	6.0	10.50	30	—	1.62432 ± 0.31968	(28)–(30)
190829A	2019oyw	Ic-BL	0.0785	$(2.0 \pm 0.3) \times 10^{50}$	6.27	18.00	0.018	—	0.794016 ± 0.0216	(31)–(32)

NOTE.—**Information on SN type** is retrieved from Transient Name Server (www.wis-tns.org) and SIMBAD Astronomical Database (<http://simbad.cds.unistra.fr/simbad/>), except for the following events: SN 2001ke: Bloom et al. (2002); SN 2009nz: Berger et al. (2002); SN 2011kl: Greiner et al. (2015); SN 2019jri: Melandri et al. (2022); SN 2019oyw: Hu et al. (2021). **References for z:** 980425: Galama et al. (1998); 011121: Infante et al. (2001); 021211: Vreeswijk et al. (2003); 030329: Thöne et al. (2007); 031203: Prochaska et al. (2003); 050525: Della Valle et al. (2006b); 060218: Pian et al. (2006); 081007A: Berger et al. (2008); 091127: Vergani et al. (2011); 100316D: Bufano et al. (2012); 101219B: Sparre et al. (2011); 111209A: Vreeswijk et al. (2011); 120422A: Schulze et al. (2014); 120714B: Fynbo et al. (2012); 130215A: Cucchiara & Fumagalli (2013); 130427A: Flores et al. (2013); 130702A: Mulchaey et al. (2013); 130831A: Cucchiara & Perley (2013); 161219B: Tanvir et al. (2016); 171010A: Kankare et al. (2017); 171205A: Izzo et al. (2017); 180728A: Rossi et al. (2018); 190114C: Selsing et al. (2019); 190829A: Valeev et al. (2019); **References for data sources:** (1) Hoefflich et al. (1998), (2) Iwanoto et al. (1999), (3) Cano et al. (2017), (4) Yamazaki et al. (2003), (5) Lyman et al. (2016), (6) Lian et al. (2022), (7) Ulanov et al. (2005), (8) Ghirlanda et al. (2004), (9) Fox et al. (2003), (10) Pandey et al. (2003), (11) Della Valle et al. (2004), (12) Amati (2006), (13) Klose et al. (2019), (14) Golenetskii et al. (2013), (15) Ruffini et al. (2019c), (16) Levan et al. (2014), (17) Vurm et al. (2014), (18) Cano et al. (2014), (19) Minaev & Pozanenko (2019), (20) Frederiks et al. (2016), (21) Frederiks et al. (2017), (22) Kumar et al. (2022), (23) Bright et al. (2019), (24) D’Elia et al. (2018), (25) Frederiks et al. (2018a), (26) Ruffini et al. (2021), (27) Ruffini et al. (2018d), (28) Hamburg et al. (2019), (29) Ruffini et al. (2019b), (30) Jordana-Mitjans et al. (2020), (31) Tsvetkova et al. (2019), (32) Hu et al. (2021).

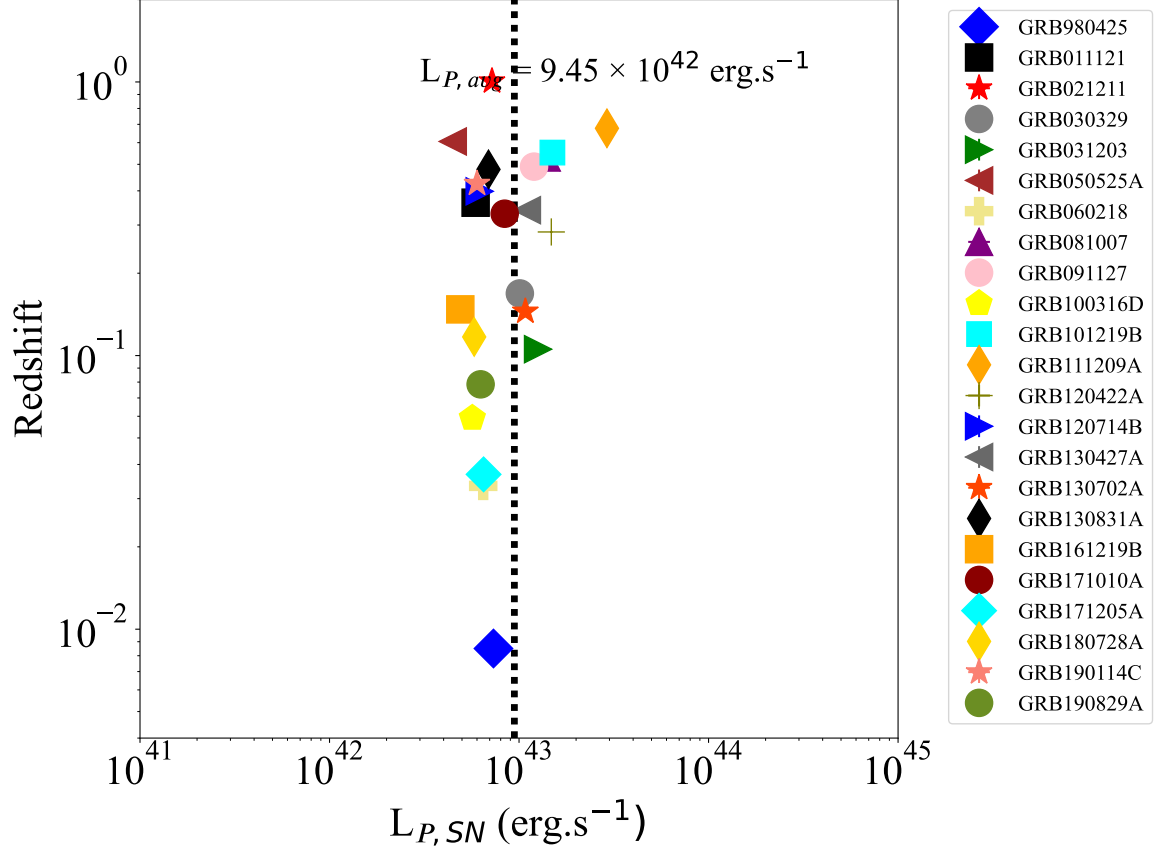


Figure 2. GRB redshifts (z) versus the values of peak luminosity of the bolometric light curve of the associated SN ($L_{P,SN}$). The plot shows the spread in data points and the lack of correlation between these two quantities.

Table 2. Physical phenomena occurring in BdHN I, II, and III, and their associated observations in the GRB data. References in the table: ^aWang et al. (2019, 2022b); Rueda et al. (2022), ^bFryer et al. (2014); Becerra et al. (2016); Becerra et al. (2022); Rueda et al. (2022); Wang et al. (2022b), ^cRuffini et al. (2019c); Moradi et al. (2021b,c), ^dBianco et al. (2001); Moradi et al. (2021c); Rastegarnia et al. (2022), ^eRuffini et al. (2019c); Rueda & Ruffini (2020); Moradi et al. (2021b); Rueda et al. (2022b), ^fRuffini et al. (2018e), ^gRuffini et al. (2018a); Wang et al. (2019); Rueda et al. (2020), ^h Cano et al. (2017) and this paper. UPE stands for ultrarelativistic prompt emission, SXFs for soft X-ray flares, HXFs for hard X-ray flares, CED for classical electrodynamics, QED for quantum electrodynamics, SN for supernova, and HN for hypernova.

Physical phenomenon	BdHN type	GRB Episodes										
		0 (SN-rise)	I (ν NS-rise)	II (NS-rise)	III (BH-rise overcritical)	IV (BH-rise undercritical)	V (BH echoes)			VI (Afterglows)		VII (SN Ic & HN)
		SN-rise (X- γ)	ν NS-rise (X- γ)	NS-rise (X- γ)	UPE (X- γ)	Jetted emission (GeV)	Cavity (X- γ)	HXF (X- γ)	SXF (X)	X Opt. Rad.	Opt. SN & HN	
CO core-collapse ^a	I,II,III	⊗										
ν NS accretion ^b	I,II,III		⊗									
NS accretion ^b	I,II			⊗								
BH QED ^d	I				⊗							
BH CED ^e	I					⊗						
BH disk accretion ^f	I						⊗	⊗	⊗			
ν NS synchr. + pulsar emission ^g	I,II,III								⊗	⊗	⊗	
Nickel decay + ejecta kinetic energy ^h	I,II,II										⊗	
		Section 5.0	Section 5.1	Section 5.1	Section 5.2	Section 5.3	Section 5.4			Section 5.5	Section 5.6	

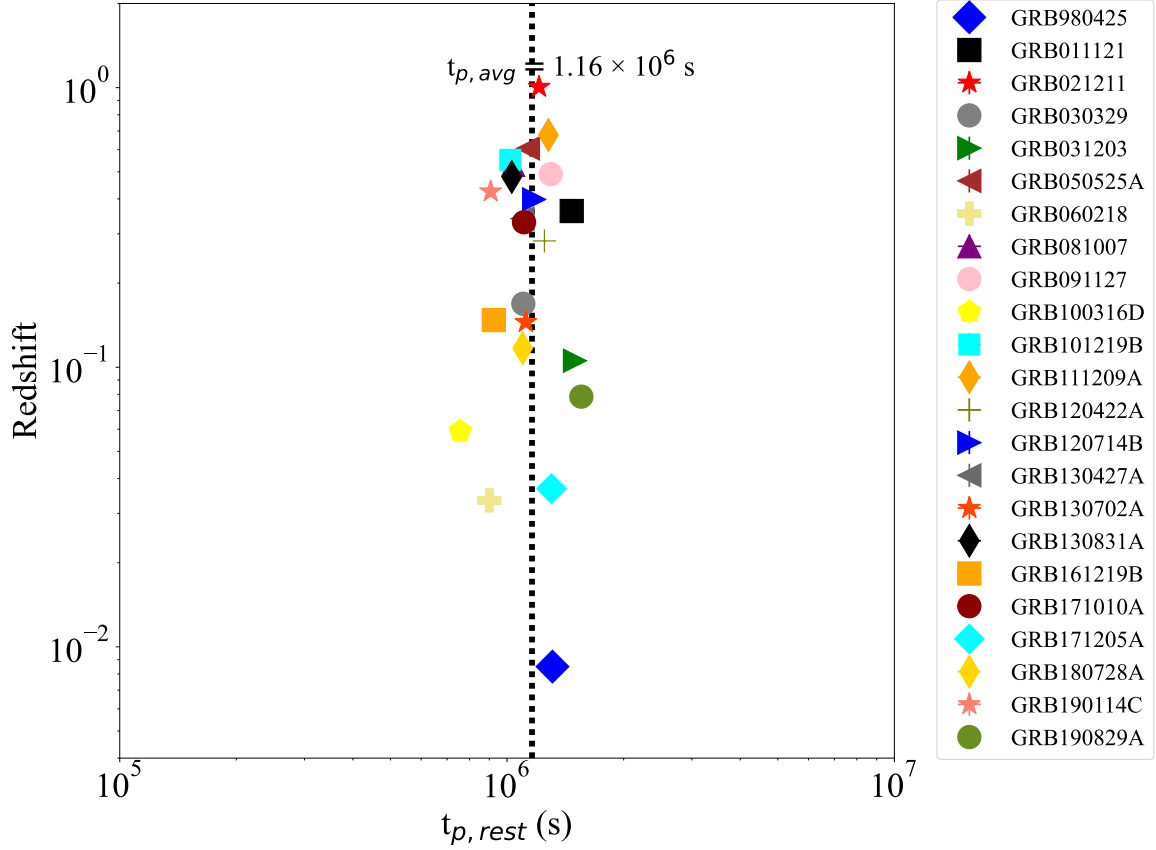


Figure 3. GRB redshifts (z) versus the peak time of luminosity of the bolometric light curve of the associated SN ($t_{p,\text{SN}}$). The plot shows the lack of correlation between these two quantities.

where n_{obs} is the photon spectrum, i.e., the number of observed photons per unit energy, area, and time.

The total energy emitted in the $[\epsilon_{\text{obs},1}; \epsilon_{\text{obs},2}]$ bandwidth per unit time, which by definition is in the source cosmological rest-frame, is

$$L_{[\epsilon_{\text{obs},1}(1+z); \epsilon_{\text{obs},2}(1+z)]} = 4\pi D_L^2(z) f_{\text{obs},[\epsilon_{\text{obs},1}; \epsilon_{\text{obs},2}]}, \quad (2)$$

where $D_L(z)$ is the source luminosity distance.

To express the luminosity L in the cosmological rest-frame energy band, $[E_1; E_2]$, common to all sources, we rewrite Eq.(2) as

$$L_{[E_1; E_2]} = 4\pi D_L^2 f_{\text{obs},[\frac{E_1}{1+z}; \frac{E_2}{1+z}]} = \quad (3)$$

$$4\pi D_L^2 k[\epsilon_{\text{obs},1}; \epsilon_{\text{obs},2}; E_1; E_2; z] f_{\text{obs},[\epsilon_{\text{obs},1}; \epsilon_{\text{obs},2}]} \quad (4)$$

where the k -correction factor is defined as

$$k[\epsilon_{\text{obs},1}; \epsilon_{\text{obs},2}; E_1; E_2; z] = \frac{f_{\text{obs},[\frac{E_1}{1+z}; \frac{E_2}{1+z}]}}{f_{\text{obs},[\epsilon_{\text{obs},1}; \epsilon_{\text{obs},2}]}} \quad (5)$$

$$= \frac{\int_{E_1/(1+z)}^{E_2/(1+z)} \epsilon n_{\text{obs}}(\epsilon) d\epsilon}{\int_{\epsilon_{\text{obs},1}}^{\epsilon_{\text{obs},2}} \epsilon n_{\text{obs}}(\epsilon) d\epsilon}. \quad (6)$$

Throughout this article, we use a Λ CDM cosmology with $H_0 = 69.6 \text{ km s}^{-1} \text{ Mpc}^{-1}$, $\Omega_M = 0.286$, $\Omega_\Lambda = 0.714$ for performing the k -correction related to the cosmological-rest frame of sources.

4. TYPE IC SUPERNOVAE ASSOCIATED WITH BDHN I, BDHN II, AND BDHN III

We address the observations of a sample of 24 spectroscopically well-identified SNe associated with long GRBs (GRB-SN). In Table 1, we give the name of the SN, the SN type, the cosmological redshift, our best estimate of the E_{iso} of the associated long GRB, the peak luminosity of the SN ($L_{p,\text{SN}}$), and the time of occurrence of the peak ($t_{p,\text{SN}}$). We also give the analogous information from the literature in the following three columns.

The optical observations are performed during the long-lived multiwavelength afterglow of each GRB. As pointed out by Cano et al. (2017, and references therein), the spectroscopic analysis of the light curve close to their maxima, through the identified presence of strong absorption/emission lines (Cappellaro 2022), allows classifying the type of the SN, e.g., Ib/c or Ic-BL. The photometric observation also indicates the evidence for an emerging SN by a characteristic rise in the opti-

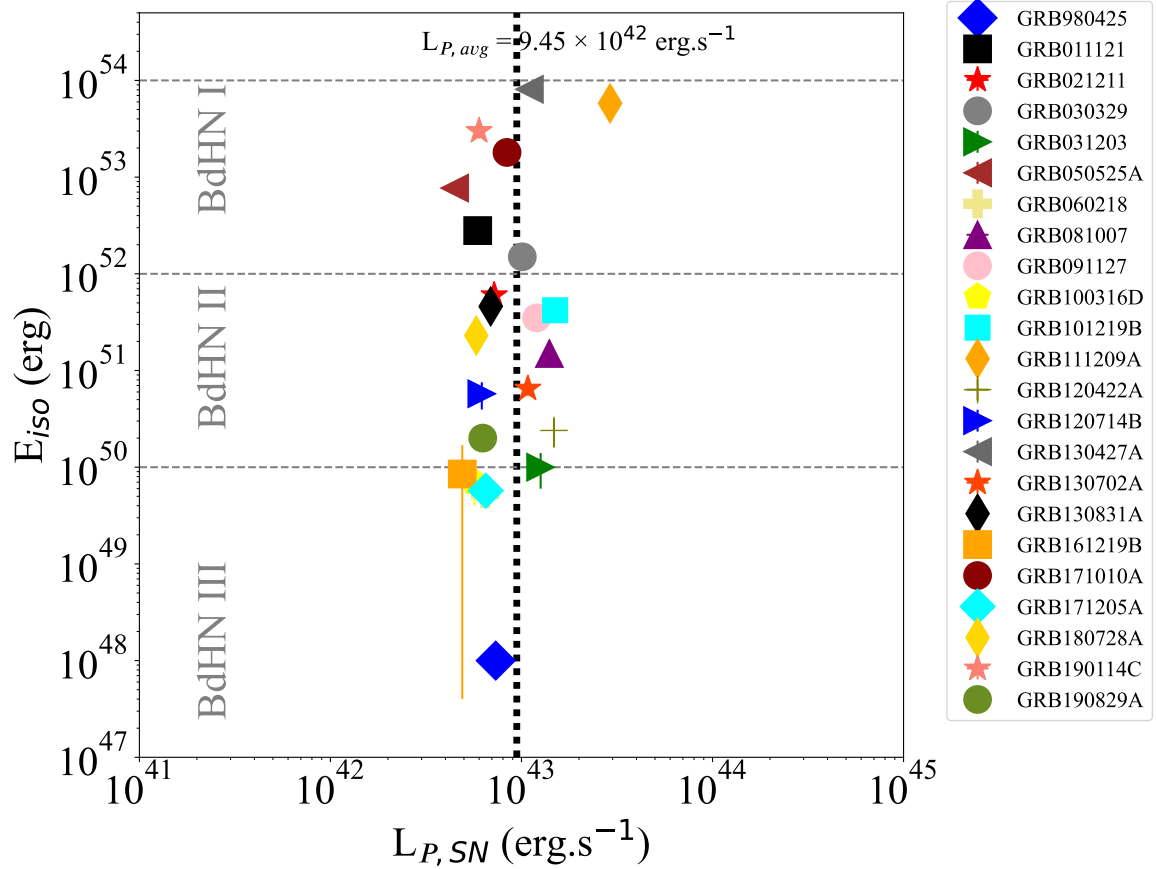


Figure 4. Isotropic-equivalent energy ($E_{\gamma,iso}$) of GRB versus the peak luminosity of the bolometric light curve of the associated SN ($L_{P,SN}$). The plot shows the lack of correlation: the SN luminosities stay within an order of magnitude spread, while the GRB energy spans ~ 6 orders of magnitude.

cal afterglow at around 7–20 days after the main GRB trigger. The rise in apparent magnitude points to the energy deposited in the expanding outflow by the decay of radioactive nickel mass synthesized during the SN explosion (see Section 5).

Since the first evidence of the GRB-SN association, GRB 980425-SN 1998bw in 1998 (Galama et al. 1998), to the end of 2019, there have been detected about 60 GRB-SN events. We collected the data from literature and catalogs (Poolakkil et al. 2021; Lien et al. 2016), Gamma-ray Coordinates Network (GCN),¹ online tables^{2,3} and databases.^{4,5} Among these associations, there are 24 SNe identified spectroscopically and 26 SNe showing only a prominent “bump” in the late op-

tical afterglow and any obtained spectra.⁶ Interestingly, half of the sample occurred within *Fermi* space observatory operational era, thus extending information to the high-energy counterpart of the accompanying GRBs (Ajello et al. 2019); see Table 1.

Due to incomplete data in some of the observed GRB-SN, we cannot use the entire population. Therefore, we further focus on the 24 spectroscopically confirmed SNe associated with GRBs to the end of 2019.

The peak luminosity integrated over the optical bands is similar in all observed SNe associated with GRBs independent of their redshift; see Fig. 2. The same applies to the time of occurrence of the peak measured since the GRB trigger and is independent of the redshift of the SN; see Fig. 3. As we will point out in Section 5, the determination of the trigger time strongly depends on the luminosity of the GRB and the instrument with

¹ <https://gcn.gsfc.nasa.gov>

² <https://www.mpe.mpg.de/~jcg/grbgen.html>

³ https://user-web.iccube.wisc.edu/~grbweb_public/index.html

⁴ <https://www.wis-tns.org>

⁵ <http://simbad.cds.unistra.fr/simbad/>

⁶ It was noted by Cappellaro (2022) that due to recent emergence of transient surveys, the current SN discovery rate is counting to about a thousand event per year. Thus, only a small fraction of them receives a spectroscopic confirmation.

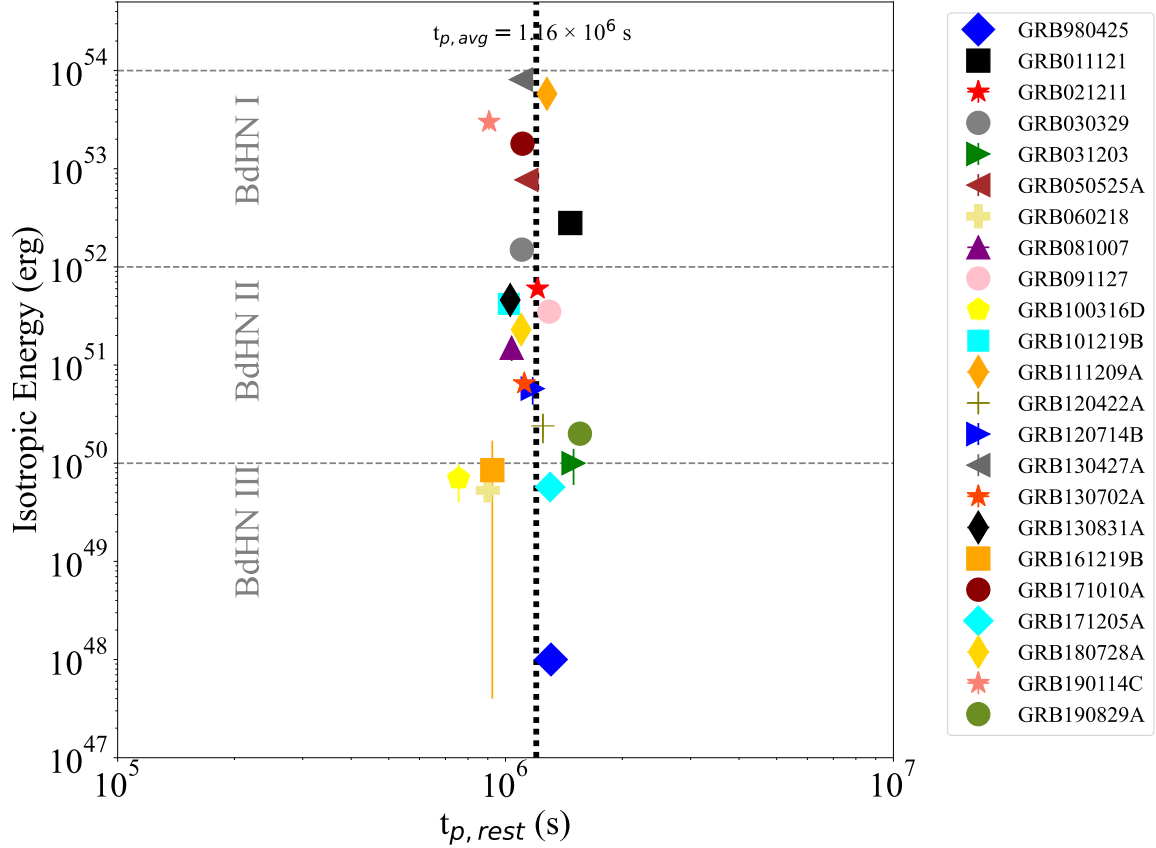


Figure 5. Isotropic-equivalent energy ($E_{\gamma, \text{iso}}$) of GRB versus the peak time of luminosity of the bolometric light curve of the associated SN ($t_{p, \text{SN}}$). The plot shows the lack of correlation: the SN peaking times (in the rest-frame) stay within an order of magnitude spread, while the GRB energy spans ~ 6 orders of magnitude.

the indeterminacy of $\sim 10^4$ s. The average peak bolometric luminosity is $L_{p, \text{avg}} = (9.45 \pm 3.8) \times 10^{42}$ erg s^{-1} and the average peaking time in the rest-frame is $t_{p, \text{avg}} = (1.16 \pm 0.24) \times 10^6$ s.

Quite apart from this universality, it follows from Figs. 4 and 5 that the peak luminosity of the associated SN Ic and its time of occurrence are not correlated to the E_{iso} of the BdHN I, II, and III.

As recalled already in the Introduction, we can conclude that the progenitors of SN Ic are composed of a $\sim 10M_{\odot}$ CO star and a $\sim 2M_{\odot}$ companion NS. As recalled in Section 2, the same progenitors also characterize the BdHNe. In both cases, the trigger is marked by the collapse of the CO core. From the results presented above, a new problem arises: how can the thermonuclear evolution of the SN Ic, characterized by a standard energy of $\sim 10^{49}$ erg, be unaffected by the presence of BdHN I, II, and III with energies in the range of $\sim 10^{49}$ – 10^{54} erg. To answer this fundamental question and the above energetic difference, we proceed in Section 5 to illustrate the physical processes in the seven fundamental episodes characterizing a most general BdHN and their spectral properties. In Sections 6–9, we provide two ex-

amples of BdHN I, one of BdHN II, and one of BdHN III.

5. BDHN EMISSION EPISODES

The advantage of introducing the BdHN model may be to bring a certain amount of clarity in a field in which a great deal of confusion exists even in interpreting the specific spectral data (see, e.g., Li 2022).

We have recalled in the Introduction the differences in addressing the fundamental question of what is considered a long GRB: in the traditional literature, the GRB is described by a single event originating from a “collapsar” and manifesting itself by an ultra-relativistic jetted emission. A much more scientifically complex and vaster picture starts from a binary progenitor.

We have also recalled how the large observational support and the equally profound theoretical comprehension following the breakthrough of the Beppo SAX promoted the unification of traditional gamma-ray astronomy to the field of X-ray astronomy. This led to an expansion to additional multi-wavelength observations. The leading conceptual progress has emerged from explaining the spatial and temporal coincidence of two

very different astrophysical events: the occurrence of SN Ic and the occurrence of long GRBs.

The BdHN model is rooted in the explanation of this coincidence, as explained in this article: we soon realized that both systems have a common origin in a progenitor composed of a CO core and a binary NS companion (see Section 1). Their evolution leads to an SN explosion which, in addition to a large amount ($7-8M_{\odot}$) of ejecta, gives origin to a millisecond pulsar at its center. We have indicated in Section 2 the crucial role of the initial large angular momentum of the CO-NS binary systems due to the short initial binary period P_{bin} . Three different BdHN types originate from very different energies: BdHN I with P_{bin} of $\sim 4-5$ min and energies ranging in $10^{52}-10^{54}$ erg, BdHN II with $P_{\text{bin}} \sim 20$ min and energies ranging $10^{50}-10^{52}$ erg, BdHN III with P_{bin} up to a few hours and energies below 10^{50} erg. Equally remarkable is the fact that the same progenitors, as shown in Table 2 and Figs. 2–5, lead to SNe Ic of a standard energy of 10^{49} erg and an HN with the kinetic energy of $\sim 10^{52}$ erg. This result points to a thermonuclear evolution of the SN Ic largely independent of the associated GRB.

The present effort is dedicated to addressing the physics and evolution of GRBs and SN Ic with quantum and classical field theories, which are currently full of conceptual holes. Within the BdHN model, we address the explanation of the above observational facts and justify the assumptions we have made. We have identified seven basic Episodes in the most general BdHN. Each Episode has been characterized through a specific new physical process, partly an extension to new extreme regimes of previously known processes or new processes introduced here for the first time. This has been made possible by observations in the extragalactic of phenomena never observed in our local Universe. Each Episode has been duly scrutinized, and the new physical laws introduced for their explanation have been validated by a time-resolved spectral analysis. The importance of these Episodes can hardly be overestimated since they offer the most reliable guide we have in classifying and interpreting the rapidly growing and already very complex observational picture. After some general considerations, we refer in the following sections to the seven specific Episodes, the related observable, and the BdHN type in which they are present. We then proceed in the following sections to specific examples; two BdHNe I in Section 6 on GRB 180720B (in Table 2 we identify the physical phenomena), on GRB 190114C in Section 7, GRB 190829A as a BdHN II in Section 8, and GRB 171205A as BdHN III in Section 9.

5.0. *The SN-rise*

As mentioned in Section 4, the BdHN process, which includes the formation of an SN Ic and the associated GRB, is triggered by the gravitational collapse of the CO core. The early detection of this event, namely the first appearance of the SN related to the CO core collapse (SN-rise), is quite rare. It depends on various factors, including the GRB energy, the distance of the source, and especially the operation of the multi-wavelength detectors at the unpredictable moment of the occurrence of the gravitational collapse. The possible examples in BdHN I are GRB 160625B (Ruffini et al. 2021) and GRB 221009A (in preparation) and, in BdHN II, GRB 190829A (see Section 8). We are progressing in determining this episode’s spectral signature, which is essential to identify the underlying physical processes originating the SN explosion.

Subsequently to the SN-rise, the hypercritical accretion of the $7-8M_{\odot}$ onto the ν NS and the NS companion shows up as Episodes of the GRB prompt emission (Becerra et al. 2016; Wang et al. 2019, 2022b; Becerra et al. 2022; Wang et al. 2022b).

5.1. *The ν NS-rise*

The prompt GRB emission starts with the transfer of energy and angular momentum due to the accretion of the SN ejecta both on a very rapidly spinning ν NS and the slower rotating companion NS. The period of the ν NS ranges from 1 ms in the case of a BdHN I to ~ 100 ms periods in the case of a BdHN III. We have indicated as ν NS-rise this first BdHN Episode. This process occurs in all three BdHNe types, with a characteristic CPL spectrum (see, e.g., Rueda et al. 2022a). In parallel to the ν NS emission, the SN ejecta accretion that occurs on the companion NS is energetically much weaker. However, in the case of BdHN I, the hypercritical accretion onto the NS companion, a few seconds after the trigger given by the ν NS-rise, leads to the formation of the BH and the new Episode of the ultra-relativistic prompt emission (UPE) occurs, with a clear CPL + thermal emission (see Section 5.2). Initially, the UPE and the ν NS-rise emissions have comparable luminosities. In the case of GRB 180720B, a first ν NS-rise I Episode, lasting 4.84 s, is followed by a prominent UPE I Episode lasting 1.21 s, both identifiable by their different spectral properties. Soon after, the ν NS-rise II Episode starts, lasting for 3.02 s, followed by the UPE II Episode for 1.82 s; see details in Table 3. What is fascinating and identifiable is the non-interference of the emission process from the ν NS-rise and the UPE. A similar behavior is present in GRB 190114C; see details in Table 4.

In both cases of GRB 180720B and GRB 190114C, the millisecond rotation of ν NS has given the possibility

of examining the equilibrium configurations of a triaxial Jacobi ellipsoid soon evolving into a Maclaurin spheroid with possible emission of Gravitational waves (Rueda et al. 2022a). Such possibility, theoretically indicated as necessary in the early evolution of the crab nebula pulsar (Ferrari & Ruffini 1969), can now be submitted to direct observations in BdHN I.

Following the ν NS-rise, which again we recall exists in all BdHN types, the synchrotron radiation emitted by the rapidly spinning ν NS, in the wavelengths ranging from X-rays to Optical to Radio gives origin to the afterglows. It is satisfactory that the afterglows are identically present in all BdHN types; see Section 5.5.

Numerical simulations show that the accretion process can be observed as a double-peak emission, where the relative time and intensity of the peaks depend on the orbital period and the angular momentum of the NS at the beginning of the accretion process (see Becerra et al. 2019, 2022, for details). The NS companion can reach the critical mass for BH formation before the second peak of fallback accretion onto the ν NS (see Becerra et al. 2019, 2022, for recent simulations). Since the accretion process and associated ν NS-rise is not exclusive of binaries forming a BH, the above double-peak emission from the accretion can appear as the prompt emission in a BdHN II, as in the case of GRB 190829A (Wang et al. 2022b). The prompt emission appears without a double-peak structure in BdHN III, like in GRB 171205A (Wang et al. 2022a); see Section 9.

We refer to Section 6 for details on the ν NS-rise in GRB 180720B, Section 7 for GRB 190114C, Section 8 for GRB 190829A, and Section 9 for GRB 171205A.

5.2. The UPE phase

The UPE phase is the first new process that has made possible the extrapolation of the well-known quantum electrodynamics (QED) process of vacuum polarization, which for a long time approached in earth-bound experiments without reaching observational support, and now observing the new regime of overcritical fields in extragalactic astrophysics sources (see Ruffini et al. 2010, and references therein).

These processes were pioneered by decades of theoretical works in the 1930s by Paul Dirac (Dirac 1930), Gregory Breit and John Archibald Wheeler (Breit & Wheeler 1934) and by Fritz Sauter (Sauter 1931a,b), Werner Heisenberg and Hans Euler (Euler 1936; Heisenberg & Euler 1936), and later in the 1940s by Julian Schwinger (Schwinger 1948, 1949a,b), and Richard Feynmann (Feynman 1948, 1949a,b); see e. g. Cherubini et al. (2009); Ruffini et al. (2010). Despite many efforts, the inverse of the Breit-Wheeler process, namely

pair creation by two photons was never observed in Earth-bound experiments neither in the past at DESY and SLAC, nor in the present in Brookhaven and Darmstadt, nor at ELI <https://eli-laser.eu/> or XFEL <https://www.xfel.eu>. It is today clear that these processes are routinely observed in GRBs on the vastest possible energy scales up to 10^{54} erg/s, on the shortest time intervals up to 10^{-9} s, and highest energies up to $\sim 10^{18}$ eV.

A novel *hierarchical (self-similar)* structure has been evidenced in the UPE spectra of GRB 190114C and GRB 180720B, composed of a black body (BB) plus a cutoff power-law (CPL) model; see sections 6 and 7. Namely, the spectra of the UPE, rebinned in time intervals up to a fraction of a second, are all fitted by analogous BB+CPL models. This feature implies a microscopic phenomenon at work on ever shorter timescales. The explanation of the UPE phase of these BdHN I require the interplay of general relativity, QED, and plasma physics in an overcritical regime, which has been observed for the first time.

In BdHN I, ionized matter and the magnetic field inherited from the collapsed NS surround the newborn Kerr BH. These three components comprise the *inner engine* that drives the GRB radiation above MeV energies, i.e., the prompt and the GeV emission (Ruffini et al. 2019c; Rueda & Ruffini 2020; Moradi et al. 2021b; Ruffini et al. 2021; Moradi et al. 2021c).

The QED process at work in the UPE originates in the vacuum polarization of the BH vicinity by the electric field, E , induced by the gravitomagnetic interaction of the Kerr BH and the magnetic field, B_0 . At the BH horizon, $r = r_H = (1 + \sqrt{1 - \alpha^2})GM/c^2$, the electric field is approximately given by (see, e.g., Ruffini et al. 2019c; Rueda & Ruffini 2020)

$$E(r_H) \sim \frac{v_H}{c} B_0 \sim \frac{\Omega_H r_H}{c} B_0 = \frac{\alpha B_0}{2} \approx \frac{Q_{\text{eff}}}{r_H^2}, \quad (7)$$

where M , J , $\alpha = cJ/(GM^2)$, and $\Omega_H = c\alpha/(2r_H)$ are, respectively, the BH mass, angular momentum, dimensionless spin parameter, and angular velocity. The last expression introduces the *effective charge* (the BH has zero net charge), defined by $Q_{\text{eff}} = (G/c^3)2B_0J$ (see Ruffini et al. 2019c; Rueda & Ruffini 2020; Moradi et al. 2021b, for details).

For a magnetic field strength $B_0 > 2B_c/\alpha_0$, or conversely, for an initial BH spin parameter $\alpha_0 \geq 2B_c/B_0$, the induced electric field is initially overcritical, i.e., $E(r_H) \geq E_c = m_e^2 c^3/(e\hbar) \approx 1.32 \times 10^{16}$ V cm $^{-1}$. Therefore, in a short time-scale of the order of the Compton time, $\sim \hbar/(m_e c^2) \approx 10^{-21}$ s, the approximate vacuum around the BH is rapidly filled with electron-positron

pairs (e^+e^-), forming an optically thick plasma. The e^+e^- pairs self-accelerate and engulf baryons from the low-density medium around the BH. The plasma reaches transparency at large distances from the BH (e.g., $R_{\text{tr}} \sim 10^9$ cm), with large Lorentz factor (e.g., $\Gamma \sim 10^2$; see [Moradi et al. 2021c](#)). There is no single transparency event, but rather a train of transparencies that continues when the electric field reaches the critical value. This occurs when the spin parameter has been reduced from its initial value, α_0 , to $\alpha \sim 2B_c/B_0$.

The e^+e^- plasma energy comes from the electric energy stored in the electric field induced by the interaction of the external magnetic field and the gravitomagnetic field of the Kerr BH. Thus, the ultimate energy reservoir is the BH extractable energy, $E_{\text{ext}} = (M - M_{\text{irr}})c^2$, where M_{irr} is the BH irreducible mass. The latter is related to the other BH parameters by the mass-energy formula ([Christodoulou 1970](#); [Christodoulou & Ruffini 1971](#); [Hawking 1971](#))

$$M^2 = \frac{c^2 J^2}{4G^2 M_{\text{irr}}^2} + M_{\text{irr}}^2. \quad (8)$$

As shown in ([Moradi et al. 2021c](#); [Rastegarnia et al. 2022](#)), each transparency process reduces the BH angular momentum by a small fractional amount $\Delta J/J \sim 10^{-9}$, leading to a slightly smaller angular momentum $J^* = J - \Delta J$. The BH mass changes by $\Delta M \approx \Omega_H \Delta J/c^2$ (keeping the BH irreducible mass approximately constant in the process), so $\Delta M/M \sim \Delta J/J$. Therefore, the system starts a new process with the same magnetic field B_0 , kept constant, and a new effective charge of $Q_{\text{eff}}^* = Q_{\text{eff}} - \Delta Q_{\text{eff}}$, with $\Delta Q_{\text{eff}}/Q_{\text{eff}} = \Delta J/J$.

We refer to Section 6 (and [Rastegarnia et al. 2022](#)) for details on the UPE phase in GRB 180720B, and Section 7 (and [Moradi et al. 2021c](#)) for GRB 190114C.

The UPE structure has been found as well in GRB 160625B ($z = 1.406$), extending from $t_{\text{rf}} = 77.72$ s to $t_{\text{rf}} = 87.70$ s, and GRB 160509A ($z = 1.17$), spanning from $t_{\text{rf}} = 4.84$ s to $t_{\text{rf}} = 8.53$ s (see ?, for more details). There, the detailed time-resolved spectral analysis of the UPE phase of GRB 160625B has been given in Table 2, Fig. 4, as well as the luminosity and the temperature of the thermal components as a function of the rest-frame time in Fig. 5. The same analysis has been carried out for the UPE phase of GRB 160509A, presented in Table 4, Fig. 8, as well as Fig. 9 of ?. Although the UPE has been successfully analyzed in both sources, we are verifying the remaining six Episodes.

5.3. High-energy jetted (GeV) emission

At the end of the UPE phase, the strength of the induced electric field is lower than the critical field's, so

the vacuum polarization's QED process is no longer active. Yet, the inner engine still induces a sufficiently large electric field to power the observed GeV emission, although by a classical electrodynamics (CED) process. The electric field accelerates charged particles that move along and spiral around the magnetic field lines given the magnetic dominance, i.e., $\mathbf{B}^2 - \mathbf{E}^2 > 0$, leading to synchrotron radiation. In particular, for a magnetic field aligned and parallel to the BH spin, electrons move outward in the polar region around the BH rotation axis ($\theta = 0$) comprised at angles $-60^\circ \lesssim \theta \lesssim 60^\circ$ in the northern hemisphere, and the analogous region in the southern hemisphere because of the reflection symmetry of the Kerr BH spacetime. For the involved pitch angles (see, e.g., [Moradi et al. 2021b](#), for details), those electrons emit most of the synchrotron radiation at GeV energies with a luminosity that explains the observed GeV radiation in (some, see below) long GRBs ([Ruffini et al. 2019c](#); [Rueda & Ruffini 2020](#); [Moradi et al. 2021b](#)). We refer the reader to [Rueda et al. \(2022b\)](#) for a fully general relativistic treatment of the above process. As for the UPE phase, the BH extractable energy powers the GeV emission, which decreases with time following a power-law with an index of $\alpha_{\text{GeV}} = -1.19 \pm 0.04$. Thus, the mass and angular momentum of the BH keeps decreasing with time. In this case, each process of emission extracts a fraction of the BH mass-energy $\Delta M/M \sim 10^{-18}$ and angular momentum $\Delta J/J \sim 10^{-16}$ (see, e.g., [Moradi et al. 2021b](#); [Rueda et al. 2022b](#)).

Unlike the isotropic afterglow emission, which originates from the ν NS and is present in *all* types of BdHN, the GeV radiation occurs only in BdHN I since the Kerr BH power it and is anisotropic, occurring in a double-cone of semi-aperture angle $\approx 60^\circ$, centered on the BH rotation axis. Therefore, it is not observable in every BdHN I, which explains the absence of observed GeV emission in a fraction of them (see [Ruffini et al. 2021](#), for details).

We refer to Section 6 for details on the GeV emission in GRB 180720B (see also [Ruffini et al. 2019c](#)), and Section 7 for GRB 190114C (see also [Rueda & Ruffini 2020](#); [Moradi et al. 2021b](#)).

5.4. The BH echoes

The hypercritical accretion onto the NS companion and the consequent BH formation in BdHN I decrease the matter density around the BH ([Becerra et al. 2019](#)). Numerical simulations show that the expanding e^+e^- plasma causes a further decrease of the density from 10^{-7} g cm $^{-3}$ to a value as low as 10^{-14} g cm $^{-3}$. The collision and partial reflection of the expanding e^+e^- plasma with the cavity walls generates emission, known

as *cavity*, characterized by a spectrum similar to a Comptonized blackbody with a peak energy of a few hundreds of keV (Ruffini et al. 2019a).

The density of the matter surrounding the newborn BH site is highly asymmetric (see Fig. 1). Consequently, the number of baryons that the e^+e^- plasma loads during its expansion have an angular dependence. The transparency of the plasma in regions with $\mathcal{B} \lesssim 10^{-2}$ explains the radiation of the UPE phase, being \mathcal{B} the baryon load parameter. The transparency in regions with $\mathcal{B} \sim 50$ and Lorentz factors of $\Gamma \lesssim 5$ explain the SXFs and HXFs (see Ruffini et al. 2018e, for numerical simulations). The emission is visible at intermediate angles between the binary plane and the rotation axis (see, e.g., Ruffini et al. 2021). We notice that low Lorentz factors $\Gamma \lesssim 5$ are indeed inferred from the time-resolved analysis of the X-ray data, which rule out any ultrarelativistic bulk motion (e.g., massive jets) of the emitter (see Ruffini et al. 2018e, for details).

We expect SXFs and/or HXFs to appear only in BdHN I since they are related to the transparency in the high-density regions of the e^+e^- plasma originated in the formation of the newborn Kerr BH (explained above in the UPE). However, the emission is not observable in every BdHN I because of the angular dependence of the emission, which becomes visible only for lines-of-sight close to the binary plane (Ruffini et al. 2018e).

5.5. Multiwavelength (X, optical, radio) afterglow

In the BdHN scenario, the synchrotron radiation generated by relativistic electrons in the ejecta expanding in the magnetized medium provided by the ν NS magnetic field, and powered by the ν NS rotational energy, explains the afterglow emission in the X-rays, optical, and radio wavelengths (Ruffini et al. 2018a; Wang et al. 2019; Rueda et al. 2020, 2022a).

Because the afterglow emission depends only on the existence of the ν NS, the SN ejecta, and the synchrotron radiation from an isotropic distribution of pitch angles is isotropic, the afterglow synchrotron emission must be present in *all* BdHNe. Indeed, the X-ray afterglow is observed in all the 380 BdHN I identified in Ruffini et al. (2021), and in all observed BdHN II and III, as shown in this article, which proves that the afterglow emission is spherically symmetric with excellent approximation. There is a further implication that comes from the nature of the BdHN progenitor: every gravitational collapse of a CO star with sufficient short orbital period must necessarily lead to a ν NS (see Conclusions).

A semi-analytic theoretical treatment of the above synchrotron emission in BdHN can be found in Rueda et al. (2022a); Wang et al. (2022b). The synchrotron

luminosity follows a power-law behavior with the same power-law index in all energy bands. The fit of the multiwavelength afterglow data with the above model gives information on the SN ejecta expansion velocity, the ν NS magnetic field, the energy and distribution of electrons in the ejecta, and the power injected by the ν NS into the SN ejecta. This description of the GRB afterglow within the BdHN scenario differs from traditional GRB models, which consider that an ultra-relativistic jet with Lorentz factor > 100 produces the prompt emission and then continues to expand, leading to the afterglow by the synchrotron emission from the accelerated electrons swept in.

In general, the X-ray emission has the contribution of the synchrotron emission and the ν NS pulsar. The ν NS pulsar luminosity is characterized by a plateau, followed by a power-law decay at times longer than the characteristic spin-down timescale. Thus, in the X-rays, the sum of the synchrotron and the pulsar emission can result in a power-law luminosity that is shallower than the power-law luminosity of pure synchrotron radiation. Therefore, from the energetics of the afterglow, and the fit of the X-ray light curve, it is possible to infer the evolution of the ν NS rotation period and magnetic field strength (see, e.g. Ruffini et al. 2018a; Wang et al. 2019; Rueda et al. 2020; Ruffini et al. 2021; Rueda et al. 2022a; Wang et al. 2022b).

5.6. The classic SN emission powered by nickel decay

Finally, the emission is observed in the optical band powered by the energy release of nickel decay (into cobalt) in the SN ejecta. We refer to Rueda et al. (2021); Rueda (2021); Rueda et al. (2019a) for recent reviews on the BdHN scenario of long GRBs and the related physical phenomena.

The nuclear energy released by the decay of nickel into cobalt within the SN ejecta powers the observed energy of the SN Ic emission. The SNe associated with GRBs are similar to each other irrespectively on the GRB energetics (see, e.g., Cano et al. 2017 and this article). The GRB-SN connection is one of the most relevant observational properties constraining GRB models. We introduce in this article additional observational features of the GRB-associated SNe and discuss how they constrain GRB models.

Therefore, within the BdHN model, the SN optical emission is always present and observable for $z < 1$ with current telescopes or $z > 1$ for future missions. Using the BdHN model, we have successfully predicted the time of occurrence and luminosity of the SN optical emission for the BdHN I, GRB 130427A (Ruffini et al. 2013), GRB 190114C (Ruffini et al. 2019b), GRB 211023A (Aimura-

to *et al.* 2021), and GRB 221009A (Aimuratov *et al.* 2022a); for the BdHN II, GRB 180728A (Ruffini *et al.* 2018d), and GRB 190829A (Wang *et al.* 2022b); for the BdHN III, GRB 171205A (Wang *et al.* 2022b).

Having given the details of the physical origin of each episode and the information about the time-resolved spectral analysis, we now turn to specific examples of two BdHN I; GRB 180720B in Section 6, and GRB 190114C in Section 7, one BdHN II; GRB 190829A in Section 8, and one BdHN III; GRB 171205A in Section 9.

6. GRB 180720B AS AN EXAMPLE OF BDHN I

GRB 180720B was detected by Fermi-GBM (Roberts & Meegan 2018), CALET Gamma-ray Burst Monitor (Cherry *et al.* 2018), Swift-BAT (Siegel *et al.* 2018), Fermi-LAT (Bissaldi & Racusin 2018) and Konus-Wind (Frederiks *et al.* 2018b), in the gamma-rays. The High Energy Stereoscopic System (H.E.S.S.) also observed this source in the 100–440 GeV bandwidth Abdalla *et al.* 2019). In the X-rays, the *Swift*-XRT started to observe the GRB afterglow from 91 s after the Fermi-GBM trigger (Siegel *et al.* 2018), MAXI/GSC at 296 s (Negoro *et al.* 2018) and NuStar from 243 ks to 318 ks (Bellm & Cenko 2018). In the optical and near-infrared, the 1.5-m Kanata telescope observed the source at 78 s from the GRB trigger time (Sasada *et al.* 2018). Complementary observations in the optical, infrared, and radio telescopes are also reported in Martone *et al.* (2018); Sasada *et al.* (2018); Itoh *et al.* (2018); Kann *et al.* (2018); Crouzet & Malesani (2018); Watson *et al.* (2018); Schmalz *et al.* (2018); Covino & Fugazza (2018); Lipunov *et al.* (2018); Jelinek *et al.* (2018); Zheng & Filippenko (2018); Sfaradi *et al.* (2018); Izzo *et al.* (2018); Abdalla *et al.* (2019). With the redshift, $z = 0.654$, identified by the Fe II and Ni II lines in the optical observations by the VLT/X-shooter telescope (Vreeswijk *et al.* 2018), the GRB 180720B isotropic energy is $E_{\text{iso}} = 5.92 \times 10^{53}$ erg (Ruffini *et al.* 2018f; Abdalla *et al.* 2019; Fraija *et al.* 2019).

GRB 180720B possesses different episodes relating to specific astrophysical processes identified in the time-resolved spectral analysis of GRB 180720B (see Moradi *et al.* 2021a; Rueda *et al.* 2022a; Rastegarnia *et al.* 2022, Table 3 and Fig. 6).

We summarize in Table 3 the name of each episode, their physical event, the duration, the spectrum, E_{iso} , and the physical phenomena originating each event. Similarly, in Fig. 6, we represent the luminosity in wavelengths ranging from radio to TeV and show the spectra corresponding to each physical process.

The ν NS-rise I. The radiation originating from the fallback of the SN ejecta onto the ν NS (Becerra *et al.* 2019, 2022). The first evidence of this episode in GRB 180720B, referred to as the ν NS-rise, extends from $t_{\text{rf}} = 0$ s to $t_{\text{rf}} = 4.84$ s time interval, with isotropic energy of $E_{\text{iso}} = (1.53 \pm 0.09) \times 10^{53}$ erg. Its spectrum is best fitted by a Band model with $E_p = 1064$ keV, $\alpha = -0.99$, and $\beta = -2.00$.

The UPE I. This episode pinpoints the first emission originating from the BH (BH-rise). The UPE I of GRB 180720B occurs from $t_{\text{rf}} = 4.84$ s to $t_{\text{rf}} = 6.05$ s. Its measured isotropic energy is $E_{\text{UPEI}}^{\text{MeV}} = (6.37 \pm 0.48) \times 10^{52}$ erg, and its spectrum is best fitted by a CPL+BB model (index $\alpha = -1.13$, cutoff energy $E_c = 2220.569$ keV, and blackbody (BB) temperature $kT = 50.31$ keV in the observer frame).

The ν NS-rise II. It spans from $t_{\text{rf}} = 6.05$ s to $t_{\text{rf}} = 9.07$ s. The isotropic energy of this phase is $E_{\nu\text{NS}}^{\text{MeV}} = (1.13 \pm 0.04) \times 10^{53}$ erg, and its spectrum is best fitted by a CPL model ($\alpha = -0.98$, and $E_c = 737$ keV, in the observer frame).

The UPE II. It is evidenced by the first significant observed GeV photon at $t_{\text{rf}} = 7.06$ s. The UPE phase is also continued during this phase (UPE II), which lasts from $t_{\text{rf}} = 9.07$ s to $t_{\text{rf}} = 10.89$ s, with isotropic energy of $E_{\text{UPEII}}^{\text{MeV}} = (1.6 \pm 0.95) \times 10^{53}$ erg. A CPL+BB model with the following model parameters of $\alpha = -1.06_{-0.01}^{+0.01}$, $E_c = 1502.5_{-87.5}^{+88.6}$ keV and $kT = 39.8_{-1.6}^{+1.6}$ keV best fits the spectrum.

The Cavity. This emission extends from $t_{\text{rf}} = 16.94$ s to $t_{\text{rf}} = 19.96$ s, with an isotropic energy of $E_{\text{CV}}^{\text{MeV}} = (4.32 \pm 0.19) \times 10^{52}$ erg, characterized by a CPL spectrum ($\alpha = -1.16$, $E_c = 607.96$ keV) with an energy of $\sim 10^{52}$ erg and a luminosity of $\sim 10^{51}$ erg s $^{-1}$.

The HXF and SXF. The HXF of GRB 180720B extends from $t_{\text{rf}} = 28.95$ s to $t_{\text{rf}} = 34.98$ s, with $L_{\text{HXF,iso}}^{\text{MeV}} = (7.8 \pm 0.07) \times 10^{51}$ erg s $^{-1}$. Its spectrum is best fitted by a CPL model with $E_c = (5.5_{-0.7}^{+0.8}) \times 10^2$ keV, $\alpha = -1.198 \pm 0.031$. The SXF occurs from $t_{\text{rf}} = 55$ s to $t_{\text{rf}} = 75$ s, with $L_{\text{SXF,iso}}^{\text{X}} = 1.45 \times 10^{50}$ erg s $^{-1}$. Its spectrum is best fitted by a PL+BB model with $\alpha = -1.79 \pm 0.23$, and $kT = 0.99 \pm 0.13$ keV; see Table 3. Because the interaction of expanding e^+e^- with the SN ejecta produces the cavity, the HXF, and the SXF, their energetics are similar to the UPE phase (see Ruffini *et al.* 2021, and references therein).

The GeV emission. The 0.1–10 GeV emission of GRB 180720B observed by Fermi-LAT starts at $t_{\text{rf}} = 7.01$ s. The highest photon energy corresponding to this GRB is 4.9 GeV, which was detected 137 seconds after the Fermi-GBM trigger (Ronchi *et al.* 2020). The luminosity rises up to $t_{\text{rf}} \sim 40$ s. After $t_{\text{rf}} \sim 40$ s the

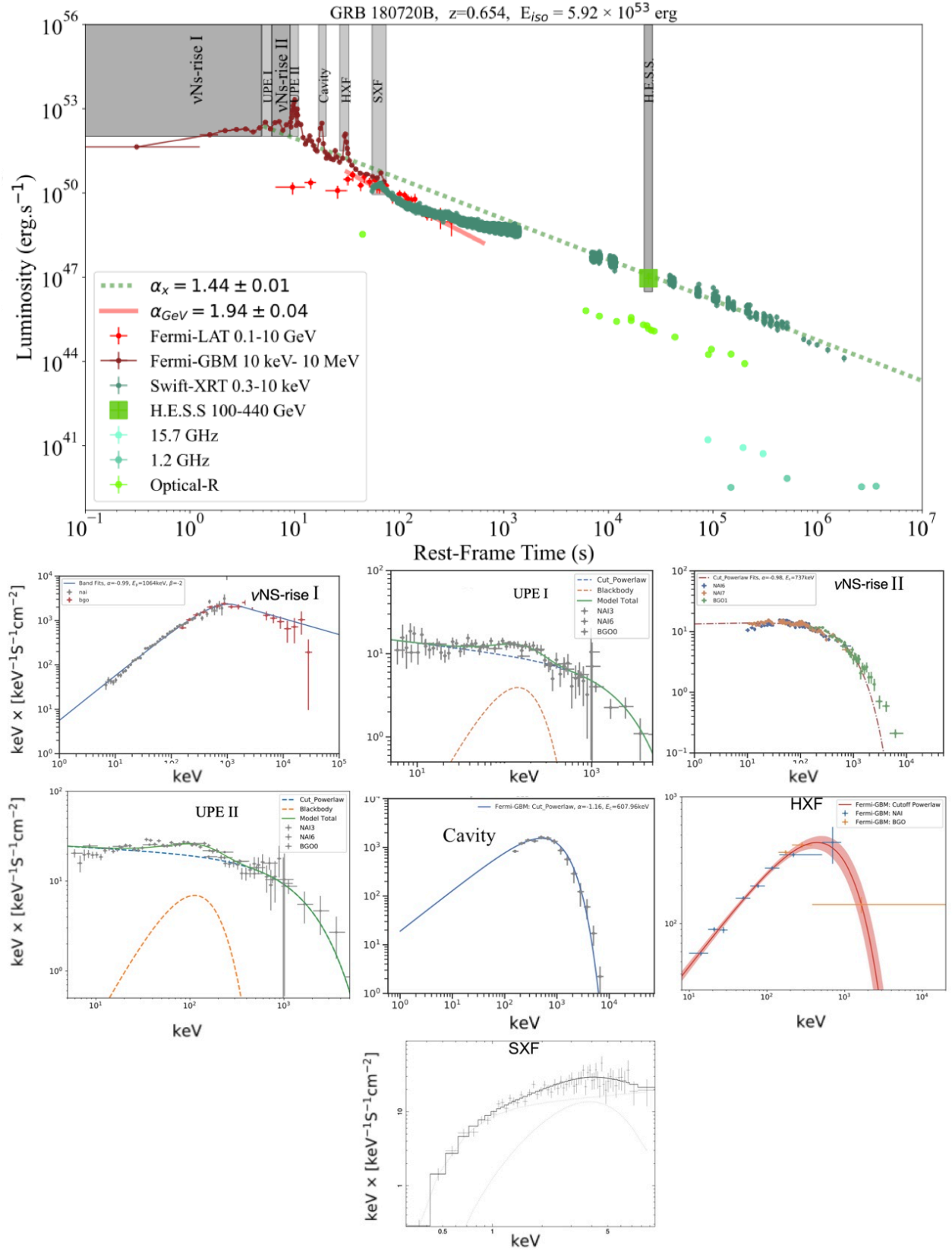


Figure 6. Luminosity light-curve of GRB 180720B and spectra related to the different Episodes identified in GRB 180720B. The energetics of the Episodes are given in Section 6 and Table 3.

Table 3. The episodes and afterglows of GRB 180720B. This table reports the name, the underlying astrophysical process, the duration (s), the best-fit spectrum, and the isotropic energy (erg) for each event in GRB 180720B. GRB 180720B has a redshift $z = 0.654$ and $T_{90}^{\text{total}} = 29.56$ s (corrected in the rest frame). The NS-rise in GRB 180720B is not observable because of the formation of the BH.

Episode	Event	duration(s)	Spectrum	E_{iso} (erg)	Physical phenomena
0	SN-rise	–	–	–	CO_{core} collapse
I	νNS-rise				ν NS accretion
	ν NS-rise I	4.84	Band	$(1.53 \pm 0.09) \times 10^{53}$	
	ν NS-rise II	3.02	CPL	$(1.13 \pm 0.04) \times 10^{53}$	
II	NS-rise	Not observable	Not observable	Not observable	Companion NS accretion
III	BH-rise (overcritical)				BH QED
	UPE I	1.21	CPL+BB	$(6.37 \pm 0.48) \times 10^{52}$	
	UPE II	1.82	CPL+BB	$(1.60 \pm 0.10) \times 10^{53}$	
IV	BH-rise (undercritical) Jettted GeV emission	600	PL	$(2.2 \pm 0.2) \times 10^{52}$	BH CED
IV	BH-echoes				BH disk accretion
	Cavity	3.02	CPL	$(4.32 \pm 0.19) \times 10^{52}$	
	HXF	6.03	CPL+BB	$(3.93 \pm 0.33) \times 10^{52}$	
	SXF	15.12	PL	$(2.89 \pm 0.42) \times 10^{52}$	
VI	The Afterglows				ν NS syn- chrotron+pulsar emission
	X-ray	10^7	PL	$(2.61 \pm 1.01) \times 10^{52}$	
	TeV	$\sim 3 \times 10^3$	PL	$(2.40 \pm 1.80) \times 10^{50}$	
	Optical	$\sim 3 \times 10^5$	PL	$(6.10 \pm 1.00) \times 10^{50}$	
	Radio	$\sim 2.21 \times 10^6$	PL	$(2.21 \pm 0.24) \times 10^{46}$	
VII	SN Ic & HN	No data	No data	No data	Nickel decay

GeV luminosity follows a temporal decaying luminosity of $L_{\text{GeV}} = 4.6 \times 10^{53} t^{-1.94 \pm 0.013} \text{ erg s}^{-1}$. It has a total isotropic energy of $E_{\text{iso,GeV}} = (2.2 \pm 0.2) \times 10^{52} \text{ erg}$.

The radio, optical, and X-ray afterglows. The X-ray afterglow luminosity observed by Swift-XRT starts at $t_{\text{rf}} = 52 \text{ s}$ with a time decaying luminosity of $L_X = 2.5 \times 10^{53} t^{-1.44 \pm 0.01} \text{ erg s}^{-1}$ and its isotropic energy is $E_{\text{iso,X}} = 2.61 \times 10^{52} \text{ erg}$. The X-ray afterglow is accompanied by the radio, optical, and TeV afterglows with isotropic energies of $E_{\text{iso,radio}} = 2.21 \times 10^{46} \text{ erg}$, $E_{\text{iso,opt}} = 6.1 \times 10^{50} \text{ erg}$, and $E_{\text{iso,TeV}} = 2.4 \times 10^{50} \text{ erg}$, respectively.

In Rueda et al. (2022a), the above afterglows of GRB 180720B have been explained within the synchrotron scenario described in Section 5.5. The X-ray afterglow of GRB 180720B exhibits two distinct power-laws, the first at times 10^2 – 10^3 s and the second at times $> 10^4 \text{ s}$ (there is a data gap at 10^3 – 10^4 s). The X-ray luminosity in the time range 10^2 – 10^3 s exhibits a shallower power-law than the pure synchrotron luminosity, as evidenced by comparing it with the power-laws of the optical and radio synchrotron at times $> 10^4 \text{ s}$. The above is explained by the contribution of the νNS magnetic-braking radiation (see Section 5.5). Around 10^2 s , the critical synchrotron radiation energy falls below the keV range, so the X-rays synchrotron luminosity decays exponentially afterward. At lower energies, the power-law behavior remains. The subsequent dominance of the pulsar emission in the observed X-ray emission has allowed us to infer the strength of the magnetic field dipole and quadrupole and the rotation period of the νNS . We refer to Rueda et al. (2022a) for more details.

The optical SN. As a BdHN I source, GRB 180720B was expected to have an associated SN emission, with an optical peak at $21.8 \pm 4.3 \text{ day}$ after the trigger (Ruffini et al. 2018f). Unfortunately, no telescope was observing the source at that time to confirm the SN appearance.

In conclusion, the total energy released by the GRB 180720B is $E_{\text{tot}} = 6.5 \times 10^{53} \text{ erg}$ of which $3.57 \times 10^{53} \text{ erg}$ is due to the BH with mass with a lower limit of $M = 2.4 M_{\odot}$ and initial spin with an upper limit of $\alpha = 0.6$. The remaining $2.93 \times 10^{53} \text{ erg}$ is due to the accreting νNS with the period of 1 ms.

7. GRB 190114C AS AN EXAMPLE OF BDHN I

GRB 190114C was first detected by the *Fermi*-GBM (Hamburg et al. 2019), and the *Neil Gehrels Swift* Burst Alert Telescope (BAT) (Gropp et al. 2019). The highest-energy GeV photon detected by *Fermi*-LAT (with a boresight angle of 68 degrees) is a 22.9 GeV event which is observed 15 s after the GBM trigger (Kocevski et al. 2019). Nordic Optical Telescope (NOT) announced the

redshift of $z = 0.424$ (Selsing et al. 2019) which leads the isotropic energy of $E_{\text{iso}} = (2.48 \pm 0.22) \times 10^{53} \text{ erg}$. The late-time 0.3–10 keV light curve observed by *Swift* X-ray Telescope (XRT) revealed a temporal power-law decay (D’Elia et al. 2019). Given the above observations, at time 15:29:54 GMT on January 15, 2019, we identified by Ruffini et al. (2019b) this GRB as a BdHN I and predicted that an optical SN should appear in the same location of the GRB within $18.8 \pm 3.7 \text{ days}$, which indeed was confirmed by Melandri et al. (2019). This successful prediction and the following detection of TeV radiation by MAGIC (Mirzoyan et al. 2019) have made GRB 190114C a prototype in which all the BdHN phases have been observed (Ruffini et al. 2019d).

The GRB 190114C reveals different episodes relating to specific astrophysical processes identified in the time-resolved spectral analysis; see Table 4 and Fig. 7.

We summarize in Table 4 the name of each episode, their physical event, the duration, the spectrum, E_{iso} , and the physical phenomena originating each event. Similarly, in Fig. 7, we represent the luminosity in wavelengths ranging from radio to TeV and show the spectra corresponding to each physical process.

The νNS -rise I. With an isotropic energy of $E_{\text{iso}} = (3.52 \pm 0.15) \times 10^{52} \text{ erg}$, it extends from $t_{\text{rf}} = 0 \text{ s}$ to $t_{\text{rf}} = 0.79 \text{ s}$ time interval. Its spectrum is best fitted by a CPL model with $E_c = 710_{-26.1}^{+21.3}$.

The UPE I. It starts from $t_{\text{rf}} = 0.79 \text{ s}$ and ends at $t_{\text{rf}} = 1.18 \text{ s}$. Its spectrum is best fitted by a cutoff power-law plus blackbody (CPL+BB) with the parameters of power-law index $\alpha = -0.62_{-0.03}^{+0.03}$, cut-off energy $E_c = 524.7_{-20.1}^{+20.1}$, temperature, $kT = 18.4_{-0.5}^{+0.5} \text{ keV}$, with isotropic energy of $E_{\text{iso}} = (1.00 \pm 0.11) \times 10^{53} \text{ erg}$.

The νNS -rise II. With an isotropic energy of $E_{\text{iso}} = (3.75 \pm 0.11) \times 10^{52} \text{ erg}$, it spans from $t_{\text{rf}} = 1.18 \text{ s}$ to $t_{\text{rf}} = 1.9 \text{ s}$ time interval. Its spectrum is best fitted by a CPL model with $E_c = 770_{-21.8}^{+22.4}$.

The UPE II. It is signed by a CPL+BB spectrum with power-law index $\alpha = -0.71_{-0.02}^{+0.02}$, cut-off energy $E_c = 717.6_{-25.4}^{+25.4}$, temperature, $kT = 111.64_{-2.5}^{+2.5} \text{ keV}$, and a self-similar structure deduced from an appropriate time-resolved analysis (Moradi et al. 2021c); see Fig. 8. With an isotropic energy of $E_{\text{iso}} = (1.47 \pm 0.20) \times 10^{53} \text{ erg}$, it starts from $t_{\text{rf}} = 1.9 \text{ s}$, and ends at $t_{\text{rf}} = 3.99 \text{ s}$. The following mass and spin parameter of the newborn BH have been inferred, $M = 4.5 M_{\odot}$, and $\alpha = 0.54$, respectively (see, e.g. Moradi et al. 2021c, for details).

The Cavity. It extends from $t_{\text{rf}} = 11 \text{ s}$ to $t_{\text{rf}} = 17 \text{ s}$. Its spectrum is best fitted by a CPL model with the photon index $\alpha = -1.67$ and the cutoff energy $E_c = 251 \text{ keV}$. The enclosure of the companion NS and the accreted material (i.e., $\approx 10^{57}$ baryons) inside the BH

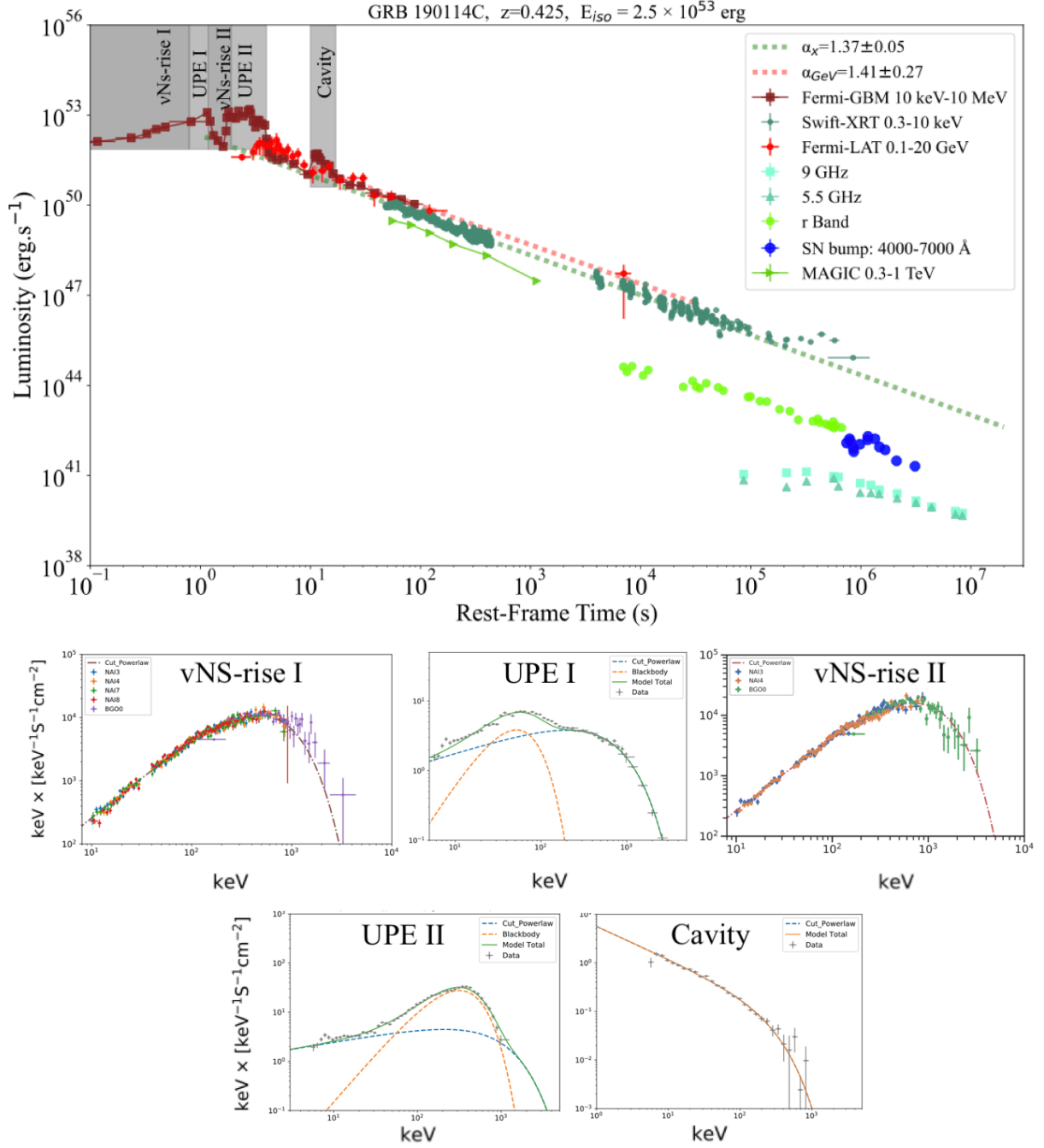


Figure 7. BdHNe I: GRB 190114C. Luminosity light-curves obtained from *Fermi*-GBM, in 10 keV–10 MeV, *Fermi*-LAT in 0.1 GeV–10 GeV, *Swift*-BAT in 15 keV–50 keV, *Swift*-XRT in 3 keV–10 keV and optical R-band. The late X-ray afterglow luminosity of BdHNe I GRB 190114C observed by *Swift*-XRT is best fit by a temporal decaying power law of $L_X = (2.5 \pm 0.4) \times 10^{53} t^{1.44 \pm 0.01} \text{ erg s}^{-1}$. The light curve of *Fermi*-LAT in is fitted by temporal decaying power law of $L_{\text{GeV}} = (4.6 \pm 2.9) \times 10^{53} t^{-1.94 \pm 0.04} \text{ erg}$. The prediction of the associated SN by (Ruffini et al. 2019b) has been successfully observed by (Melandri et al. 2019) and has made GRB 190114C as a prototype of BdHNe I (Moradi et al. 2021c) to study the properties of GRB-SN sources. The rest-frame visual absolute magnitude of the SN associated with GRB 190114C is ~ -18 mag Melandri et al. (2019), which is ~ 1 mag less than famous SN 1998bw (Patat et al. 2001). This fainter brightness can be due to the extinction of this event (Kann et al. 2019). The energetic of the Episodes are given in section 7 and Table 4.

Table 4. The episodes and afterglows of GRB 190114C. This table reports the name, the underlying astrophysical process, the duration (s), the best-fit spectrum, and the isotropic energy (erg) for each event in GRB 190114C. GRB 190114C has a redshift $z = 0.424$ and $T_{90}^{\text{total}} = 81.4$ s (corrected in the rest frame).

Episode	Event	duration(s)	Spectrum	E_{iso} (erg)	Physical phenomena
0	SN-rise	—	—	—	CO_{core} collapse
I	νNS-rise				ν NS accretion
	ν NS-rise I	0.79	CPL	$(3.52 \pm 0.15) \times 10^{52}$	
	ν NS-rise II	0.84	CPL	$(3.75 \pm 0.11) \times 10^{52}$	
II	NS-rise	Not observable	Not observable	Not observable	Companion NS accretion
III	BH-rise (overcritical)				BH QED
	UPE I	0.39	CPL+BB	$(1.00 \pm 0.11) \times 10^{53}$	
	UPE II	2.09	CPL+BB	$(1.47 \pm 0.20) \times 10^{53}$	
IV	BH-rise (undercritical)				BH CED
	Jetted GeV emission	600	PL	$(1.8 \pm 1.3) \times 10^{53}$	
IV	BH-echoes				BH disk accretion
	Cavity	13.1	CPL	$(2.49 \pm 0.12) \times 10^{52}$	
	HXF	—	—	—	
	SXF	—	—	—	
VI	The Afterglows				ν NS synchrotron+pulsar-like emission
	X-ray	$\sim 10^7$	PL	$(3.20 \pm 1.28) \times 10^{52}$	
	TeV	$\sim 3 \times 10^3$	PL	$(4.00 \pm 1.80) \times 10^{51}$	
	Optical	$\sim 3 \times 10^5$	PL	$(7.10 \pm 1.20) \times 10^{50}$	
	Radio	$\sim 2 \times 10^6$	PL	$(3.31 \pm 0.34) \times 10^{46}$	
VII	SN Ic & HN	$\sim 10^7$	BB	3×10^{49}	Nickel decay
	$M_{\text{ej}} = (6.0 \pm 4.0) M_{\odot}$				
	$M_{\text{Ni}} = (0.4 \pm 0.2) M_{\odot}$				
	$E_K = (2.5 \pm 1.8) \times 10^{52}$ erg				

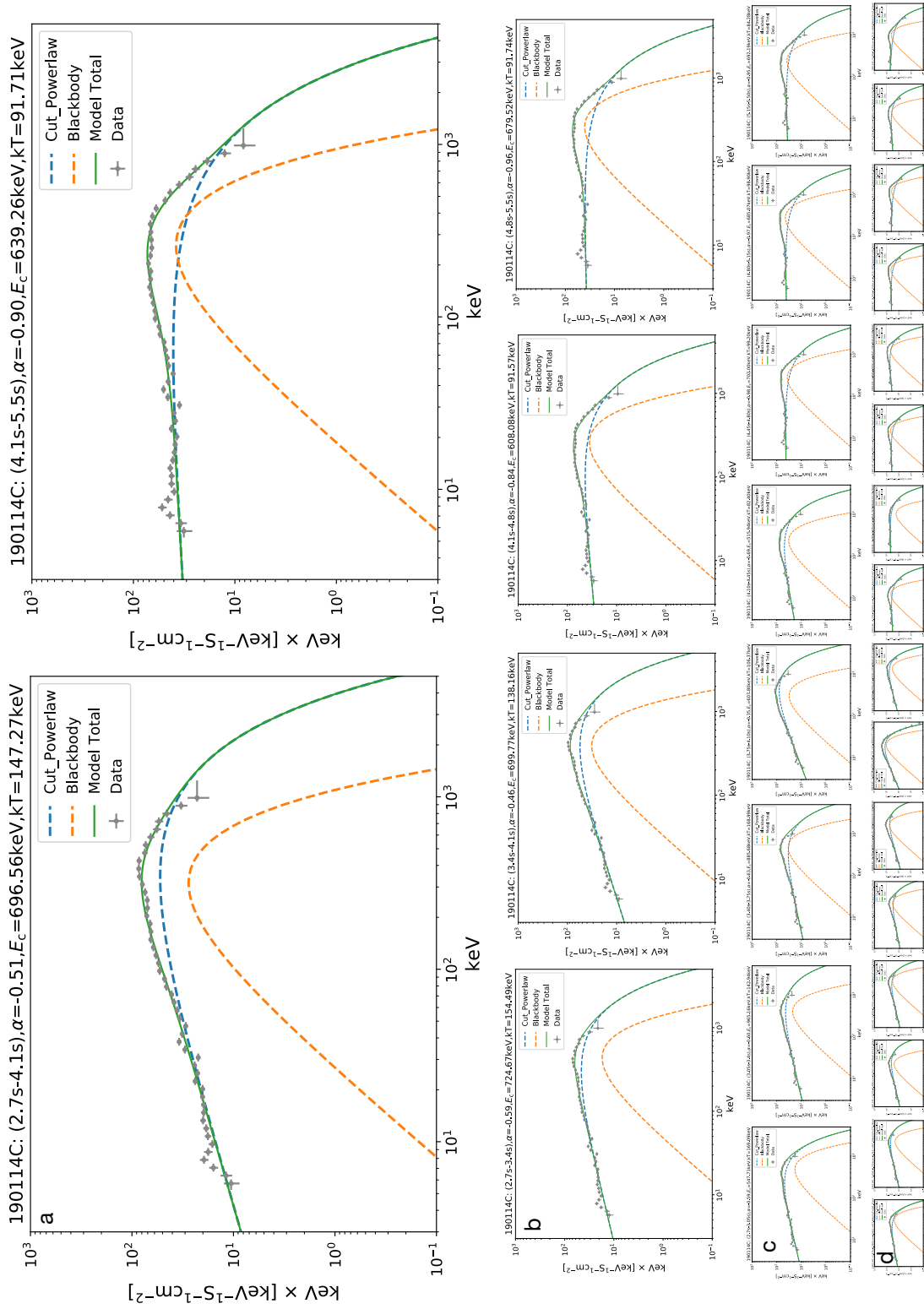


Figure 8. Time-resolved spectral analysis of UPE II phase of GRB 190114C from $t = 2.7 \text{ s}$ ($t_{\text{rf}} = 1.9 \text{ s}$) to $t = 5.5 \text{ s}$ ($t_{\text{rf}} = 3.9 \text{ s}$). The self-similar spectral structure is present when (a) the time interval is divided into two parts, (b) four parts, (c) eight parts, and (d) sixteen parts, respectively. The plot is adapted from Ruffini et al. (2019d) with the authors' permission.

horizon creates a large cavity of $\approx 10^{11}$ cm around it. The density distribution around the newborn BH has been inferred in Ruffini et al. (2019a), and the data have confirmed the spatial extension of the cavity (see Table 4 and Fig. 7).

The HXF and SXF. It is demonstrated in Ruffini et al. (2018g) and Ruffini et al. (2021) that the HXF and SXF are observable when the BdHNe viewing angle is closed to the equatorial plane of the binary progenitors. GRB 190114C is a BdHNI observed with a viewing angle orthogonal to the orbital plane of the GRB binary (Ruffini et al. 2021). Therefore, the HXF and SXF of GRB 190114C are not observable from the polar axis.

The GeV emission. The onset of the GeV radiation is also signed by the first GeV photon in the range 0.1–100 GeV observed by *Fermi*-LAT. The total energy emitted by this source in the above GeV range is $E_{\text{GeV}} = (1.8 \pm 0.9) \times 10^{53}$ erg (Ruffini et al. 2021), comparable to the energy observed by the GBM.

The radio, optical, and X-ray afterglows. The X-ray afterglow luminosity observed by Swift-XRT starts at $t_{\text{rf}} = 52$ s with a temporal decaying luminosity of $L_X = 5.14 \times 10^{52} t^{-1.37 \pm 0.05}$ erg s $^{-1}$ and its equivalent isotropic energy is $E_{\text{iso},X} = 3.2 \times 10^{52}$ erg. The X-ray afterglow of GRB 190114C is accompanied by the radio, optical, and TeV afterglows with isotropic energies of $E_{\text{iso,radio}} = 3.31 \times 10^{46}$ erg, $E_{\text{iso,opt}} = 7.1 \times 10^{50}$ erg, and $E_{\text{iso,TeV}} = 4.0 \times 10^{51}$ erg, respectively. These afterglows originated from synchrotron radiation powered by the interaction of the ν NS, with an initial period of $P_0 = 1$ ms, and the SN ejecta Rueda et al. (2022a) (see Table 4 and Fig. 7).

The optical SN. The optical signal of SN 2019jrl, a typical GRB-associated SN Ic (see Figs. 5 and 2), peaks at $\sim 10^6$ s (see also Fig. 7). Deducing certain physical properties of SN 2019jrl is difficult due to the relatively low quality of the light curve and spectra (see, e.g., Melandri et al. 2022). Therefore, we use the average values reported in Cano et al. (2017) obtained using the nickel radioactive-heating model for the bolometric SN light curve (Arnett 1982). The corresponding total SN ejected mass, nickel mass, and SN kinetic energy are, respectively, $M_{\text{ej}} = 6.0 \pm 4.0 M_{\odot}$, $M_{\text{Ni}} = 0.4 \pm 0.2 M_{\odot}$, and $E_K = (2.5 \pm 1.8) \times 10^{52}$ erg (Cano et al. 2017).

In conclusion, the total energy released by the GRB 180720 is $E_{\text{tot}} = 3.8 \times 10^{53}$ erg of which 1) 2.7×10^{53} erg is due to the BH with mass with a lower limit of $M = 4.53 M_{\odot}$ and initial spin with an upper limit of $\alpha = 0.54$, 2) 1.1×10^{53} erg is due to the accreting ν NS with the period of 1 ms, and 3) 3×10^{49} erg is due to the optical SN emission corresponding to the HN ejecta with the kinetic energy of 2.5×10^{52} erg.

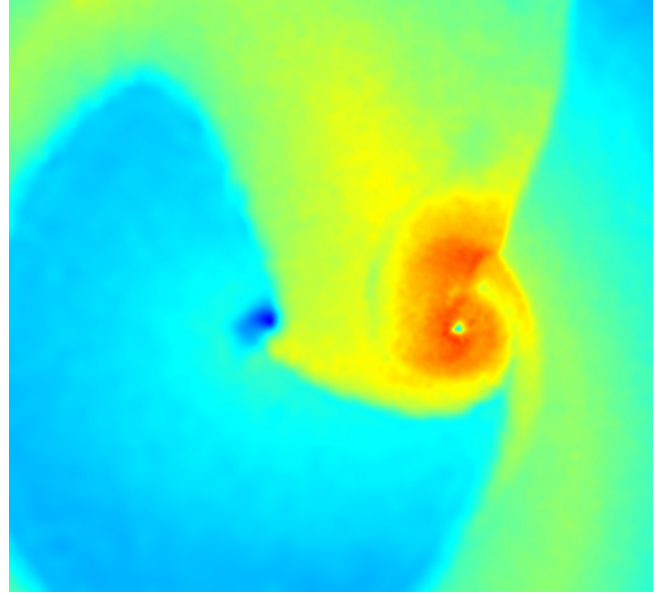


Figure 9. Ongoing accretion process of SN ejecta onto the ν NS and the NS companion, simulated in Becerra et al. (2019). The ν NS is located at the center of the dark blue spot accumulating material around it. And at the center of the green spot, the NS companion is also accreting SN ejecta. Also, we notice that a portion of the SN ejecta is flowing back towards ν NS due to the distortion of SN ejecta caused by the companion NS.

8. GRB 190829A AS AN EXAMPLE OF BDHN II

GRB 190829A triggered the *Fermi*-GBM at 19:55:53 UT on 2019 August 29 (Fermi GBM Team 2019). *Swift*-BAT was triggered 51 s later. The *Swift*-XRT started observing 148.3 s later after the Fermi trigger (Dichiara et al. 2019). *Swift*-UVOT (Dichiara et al. 2019), Half Meter Telescope (HMT) (Xu et al. 2019), Nordic Optical Telescope (NOT) (Heintz et al. 2019) and GTC Hu et al. (2021) detected the redshift of $z = 0.0785 \pm 0.005$, as one of the nearest GRBs. The flattening of the optical light-curve observed by (Perley & Cockeram 2019a; Bolmer et al. 2019; Perley & Cockeram 2019b) provided the initial evidence for the optical SN emergence. Finally, the confirmation of an associated Type Ic-BL SN named SN 2019oyw came from the spectroscopic observation performed by de Ugarte Postigo et al. (2019).

The SN-rise is not observed for this source. Two pulses are observed both in the Fermi-GBM and The *Neil Gehrels Swift*-BAT light curves (Wang et al. 2022b). The initial pulse rises at time -0.70 s, peaks at 1.02 s, and declines at time 7.46 s. After a time delay of 35.65 s, the second, more luminous pulse begins at 43.11 s, peaks at 47.89 s, and declines at 59.34 s. All the times are indicated in the rest frame. A cutoff power-law function best fits the first pulse, it has isotropic en-

Table 5. The episodes of GRB 190829A. The episodes of accretion onto the companion star and the ν NS are triggered by SN explosion. According to the BdHN terminology, they can be classified as sub-episodes of SN-rise. Times are measured in the source rest frame.

Episode	Event	duration(s)	Spectrum	E_{iso} (erg)	Physical phenomena
0	SN-rise	–	–	–	CO _{core} collapse
I	νNS-rise	16.23	Band	$(3.5 \pm 0.5) \times 10^{50}$	ν NS accretion
II	NS-rise	8.16	CPL	$(4.2 \pm 1.0) \times 10^{49}$	Companion NS accretion
III	BH-rise (overcritical)	–	–	–	BH QED
IV	BH-rise (undercritical)	–	–	–	BH CED
IV	BH-echoes	–	–	–	BH disk accretion
VI	The Afterglows				ν NS synchrotron+pulsar-like emission
	X-ray	$> 10^7$	PL	$> 4 \times 10^{50}$	
	TeV	$\sim 2 \times 10^5$	PL	$> 3 \times 10^{49}$	
	Optical	$> 10^7$	PL	$> 4 \times 10^{48}$	
	Radio	$> 10^7$	PL	$> 10^{44}$	
VII	SN Ic & HN $M_{\text{ej}} = 5.67 \pm 0.72 M_{\odot}$ $M_{\text{Ni}} = 0.5 \pm 0.1 M_{\odot}$ $E_K = (1.35 \pm 0.51) \times 10^{52}$ erg	$\sim 10^7$	BB	$> 3 \times 10^{49}$	Nickel decay

ergy $4.25 \pm 1.02 \times 10^{49}$ erg s^{−1} and averaged luminosity $4.84 \pm 1.16 \times 10^{48}$ erg s^{−1}. The second pulse shows a Band function spectrum. It is nearly one order of magnitude more energetic than the first pulse, with isotropic energy $3.56 \pm 0.50 \times 10^{50}$ erg and an averaged luminosity is $(2.05 \pm 0.29) \times 10^{49}$ erg s^{−1}; see Table 5 for the summary of the GRB 190829A episodes.

The accretion onto the NS companion and the enhanced fallback accretion onto the ν NS are responsible for the above two pulses. The comparison of GRB 190829A, especially the time separation between two pulses (~ 50 s), with several CO-NS binaries simulated in [Becerra et al. \(2019\)](#) and [Becerra et al. \(2022\)](#), indicates as the possible progenitor of this GRB a binary composed of a CO star and an NS with an orbital period in the range 20–40 min.

Figure 9 shows the visualization of the three-dimensional numerical simulation that shows the ν NS and the NS companion surrounded by high-density material and undergoing their corresponding accretion processes.

The first peak corresponds to the SN ejecta accretion onto the companion NS; see details in [Wang et al. \(2022b\)](#). A part of the ejecta is altered by the companion NS and flows back to the ν NS, leading to a second fallback accretion episode onto the ν NS, leading to the second peak.

At the time > 100 s, the afterglow started and was observed by Swift-XRT for the soft X-ray band, GTC for the optical band, and AMI-LA for the radio band, as

shown in figure 10. The X-ray afterglow from ~ 1000 s follows a power-law decay with an index of ~ -1.1 . A single power-law function best fits its spectrum with a photon index ~ -2.15 . The optical and radio light curves share similar power-law behavior. The total energy released till 10^7 s is $\sim 4 \times 10^{50}$ erg. We attribute this energy to the rotational energy of the ν NS, which leads to an initial period of 8 ms ([Wang et al. 2022b](#)).

In addition, the ejected mass by the CO core collapse, $M_{\text{ej}} = 5.67 \pm 0.72 M_{\odot}$, contributes in three different ways: 1) in spinning up the ν NS, which then releases dipole and/or multipole radiation; 2) in the accretion on the NS; and 3) in the kinetic energy, $E_K = (1.35 \pm 0.51) \times 10^{52}$ erg, of the remaining SN ejecta moving with mildly relativistic velocities. All these three components contribute to the overall energetics, which reaches its peak emission within the first 100 s.

The optical emission of the SN Ic 2019oyw, due to a nickel mass of $M_{\text{Ni}} = (0.5 \pm 0.1) M_{\odot}$, commonly occurs around $\sim 10^6$ s with the emission of 10^{49} erg; see Figs. 2–5, (see [Cano et al. 2017](#); [Hu et al. 2021](#), for an in-depth discussion of the SN observation and calculations).

The remaining kinetic energy of expansion of the ejecta leads to establishing the HN associated with GRB 190829A with the total energy of 1.35×10^{52} erg kinetic energy+all the radiation energy).

In addition to being a very close GRB at $z = 0.0785$, which has allowed a specially significant data analysis of GRB 190829A, one of the remarkable peculiarities of this source, has been the discovery of the TeV emis-

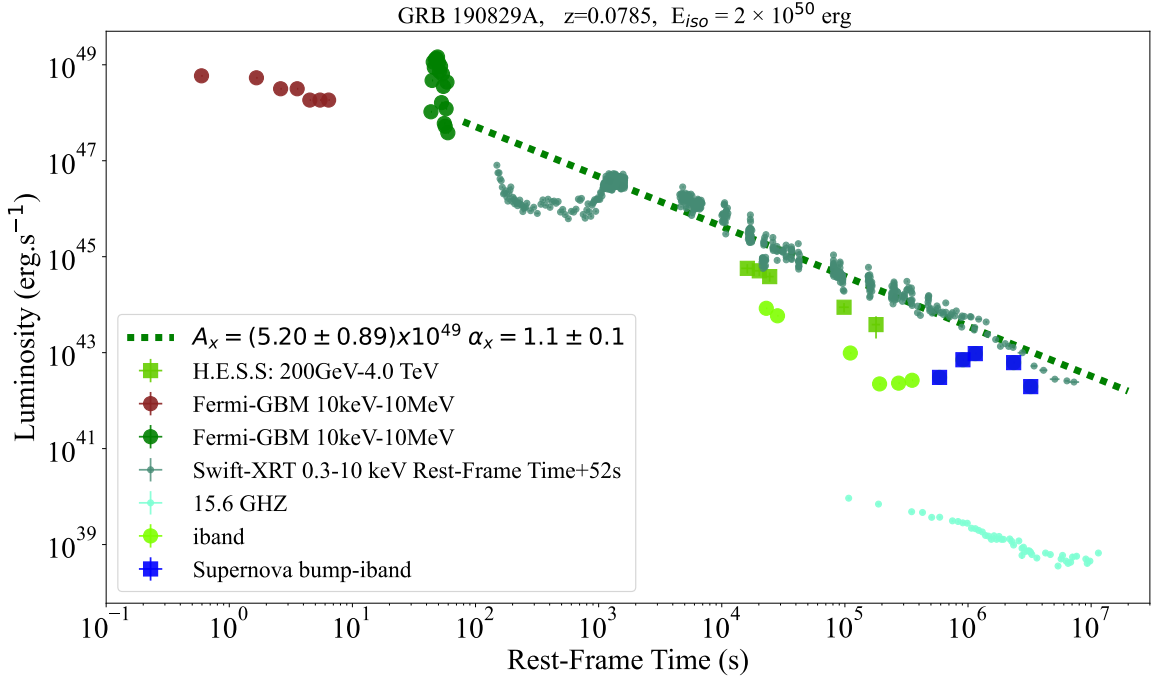


Figure 10. BdHN II: GRB 190829A. Luminosity light-curves obtained from H.E.S.S. in 200 GeV – 4 TeV, *Fermi*-GBM in 10 keV–10 MeV, *Swift*-BAT in 15–50 keV, *Swift*-XRT in 3–10 keV and i band and radio band. An SN component at $\sim 10^6$ is indicated as the blue color. The power-law fitting of the X-ray, shown as a green dotted line, gives a power-law index of -1.1 . The T_0 is taken from the trigger of *Fermi*-GBM to which the initial time of other telescopes is aligned.

sion very similar to the case of GRB 180720B and GRB 190114C. In both systems, the TeV emission behavior closely follows the 10% level of the X-ray emission. This is the most significant since no BH is present in this source, and we can generally infer that the TeV radiation is very likely associated with the ν NS activity. We can now conclude that the total energy of BdHN 190829A, observed in KeV, sub-MeV, TeV, optical, and radio bands is $E_{\text{tot}} > 8.5610^{50}$ erg.

9. GRB 171205A AS AN EXAMPLE OF BDHN III

At 07:20:43 UT, GRB 171205A (*Swift* trigger 794972) with T_{90} of 189.4 ± 35.0 s and $z = 0.0368$ (Izzo et al. 2017), was triggered and located by the *Swift* Burst Alert Telescope (BAT) (D’Elia et al. 2017; Barthelmy et al. 2017). The *Swift*-XRT (Kennea et al. 2017) and *Swift*-UVOT (GCN22181) started the observation after 134 s and 154 s, respectively, from the BAT trigger.

The prompt emission maintains its luminosity of $10^{46} - 10^{47}$ erg s $^{-1}$ for ~ 100 s then drops following a power-law, see figure 11. Its spectrum is best fitted by a cutoff power-law function with peak energy 148.55 ± 121.97 keV and low-energy power-law index -1.10 ± 0.35 . The total isotropic energy within the T_{90} of BAT gives $E_{\text{iso}} = (1.71 \pm 0.35) \times 10^{49}$ erg, see Wang et al. (2022b) and table 6 for details.

As we discussed in the previous section for BdHN II, there are three episodes of accretion, and the last two are unique features of BdHNe. In the case of GRB 171205A, the progenitor system is a single CO star or a CO-NS binary with negligible interaction between the binary components because of a large orbital separation. Hence, only the first fallback accretion onto the ν NS is expected. We also discussed that a large part of the energy from the accretion propagates inside the SN ejecta and accelerates its outermost layer, which has a steep density gradient, to a mild-relativistic speed of Lorentz factor < 10 . The fast-moving material produces the luminosity of $< 10^{47}$ erg s $^{-1}$ for some minutes, which is often missed by *Fermi*-GBM or *Swift*-BAT. But for GRB 171205A, one of the nearest GRBs at redshift $z = 0.0368$, this weak signal is resolvable and detected by *Swift*-BAT, shown as the initial hundreds of seconds of prompt emission. This physical picture is similar to the hot cocoon, which is produced by a narrow jet passing through the shells of the progenitor (see, e.g. Mészáros & Rees 2001; Ramirez-Ruiz et al. 2002; Zhang et al. 2004; Nakar & Piran 2017). The difference comes from the outflow in our picture having a clear accretion origin onto the ν NS, which emits radiation at a wider opening angle. The heated SN ejecta emits thermal emissions, a temperature of ~ 80 eV is observed by *Swift*-XRT in the initial ~ 400 s (see Fig. 2 in Wang

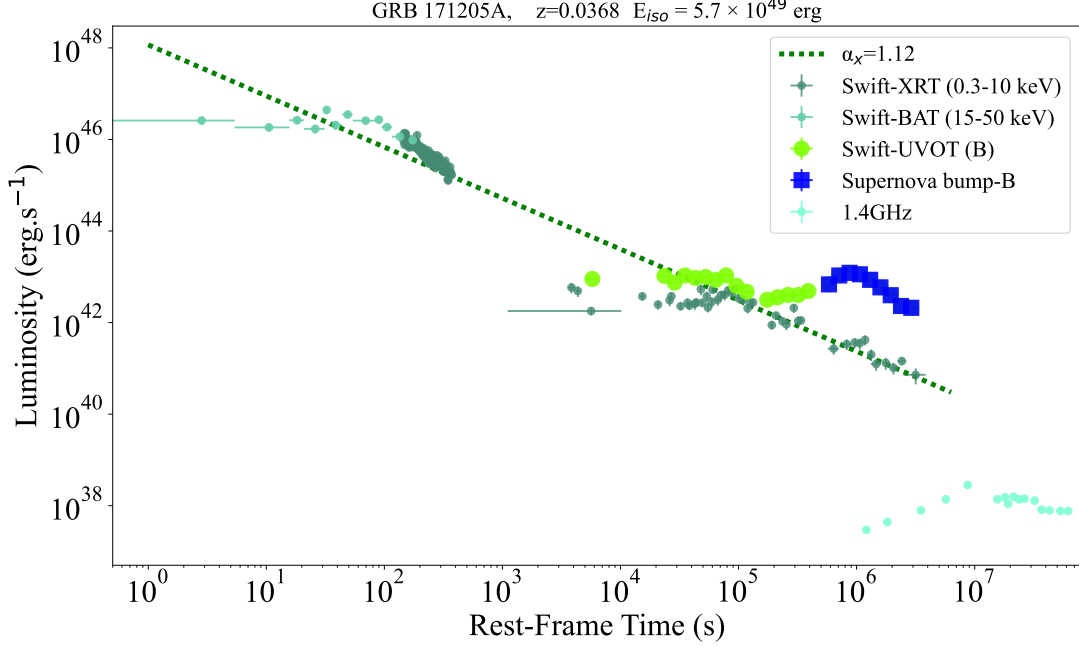


Figure 11. BdHN III: GRB 171205A. Luminosity light-curves obtained from *Swift*-BAT in 15–50 keV, *Swift*-XRT in 3–10 keV and *Swift*-UVOT in V and B band. After $t_{\text{rf}} \sim 10^5$ s it follows a decaying power-law with index $\alpha_x = 1.12 \pm 0.08$ and amplitude of $A_x = (1.1 \pm 0.8) \times 10^{48}$ erg s $^{-1}$. The optical and radio data were taken from D’Elia et al. (2018) and Maity & Chandra (2021), and the X-ray data were retrieved from the Swift-XRT repository. The blue color indicates an SN bump.

et al. 2022b), then cools to optical bands observed by *Swift*-UVOT, VLT/X-shooter, and GTC/OSIRIS.

Different from more luminous GRBs, the emission from the accelerated fast-moving material has an obvious impact on the observation of the weak GRB 171205A. Before the transparency time $\sim 10^5$ s of the fast-moving material of mass $\sim 10^{-2} M_\odot$, the X-ray and optical light-curves form a long plateau phase (see Fig. 11). The growing transparent part of the fast-moving material dominates the X-ray flux through the synchrotron mechanism, and the thermal radiation from the rest opaque part dominates the optical flux. After $\sim 10^5$ s, the X-ray light curve decays as a typical power-law of power-law index ~ -1 , and optical emission starts to be taken over by the emission from the radioactive decay of SN ejecta. The 1000 days radio observation by uGMRT (Maity & Chandra 2021) shows the radio flux rises till $\sim 10^7$ then decays as a power-law, and no jet break signature was observed, indicating the outflow has a wide opening angle. Like GRB 190829A, the same synchrotron simulation for the fast-moving material was applied on GRB 171205A (Wang et al. 2022b). To fit the power-law decay behavior of the X-ray and radio afterglow, a ν NS with an initial magnetic field of $\sim 3 \times 10^{13}$ G and a spin period of 58 ms is required (see Fig. 5 in Wang et al. 2022b).

The optical signal of SN 2017iuk, a typical GRB-associated Ic SN (see Figs. 2, 5 and 11), peaks at

$\sim 10^6$ s. Using the nickel radioactive-heating model for the bolometric SN light curve, the estimated total SN ejected mass, nickel mass, and total SN kinetic energy are $M_{\text{ej}} = 4.9 \pm 0.9 M_\odot$, and $M_{\text{Ni}} = 0.18 \pm 0.01 M_\odot$, $E_K = (2.4 \pm 0.9) \times 10^{52}$ erg, respectively, comparable to the average value deduced for the GRB-SN sample (Arnett 1982; Cano et al. 2017; Izzo et al. 2019).

10. NEW PHYSICS REGIMES IN HYPERNOVAE AND GRBS PHYSICS

The above description of the richness of physical phenomena triggered by the SN in the BdHN brings us to new physics in the explanation of long GRBs and which deserves to be highlighted. Below, we summarize new physics regimes made possible by understanding long GRBs and HNe.

10.1. Evidence from triaxiality in the ν NS early evolution

The ν NS-rise and the afterglow emission are powered by the rotational energy of the ν NS. The recent analysis of the ν NS parameters and energetics in GRB 180720B and GRB 190114C (Rueda et al. 2022a), has shown that the ν NS at the beginning of the ν NS-rise, is characterized by a rotation period at the verge of the bifurcation point of the Maclaurin sequence of equilibrium spheroids into the Jacobi ellipsoidal sequence. The presence of the

Table 6. The episodes of GRB 171205A. The first episode of prompt emission contains energy from the fallback accretion onto the ν NS and the emission from the heated SN ejecta; the latter contributes the most energy. The optical afterglow emission is dominated by the cooling of fast-moving ejecta and the supernova nickel radioactive decay. The synchrotron emission mainly contributes to the X-ray and radio bands.

Episode	Event	duration(s)	Spectrum	E_{iso} (erg)	Physical phenomena
0	SN-rise	–	–	–	CO _{core} collapse
I	νNS-rise	182.5	CPL	$(1.7 \pm 0.4) \times 10^{49}$	ν NS accretion
II	NS-rise	–	–	–	Companion NS accretion
III	BH-rise (overcritical)	–	–	–	BH QED
IV	BH-rise (undercritical)	–	–	–	BH CED
IV	BH-echoes	–	–	–	BH disk accretion
VI	The Afterglows				ν NS syn- chrotron+pulsar emission
	X-ray	$> 10^8$	PL	$> 1 \times 10^{48}$	
	Optical	$> 10^8$	PL	$> 2 \times 10^{47}$	
	Radio	$> 10^8$	PL	$> 10^{44}$	
VII	SN Ic & HN $M_{\text{ej}} = 4.9 \pm 0.9 M_{\odot}$ $M_{\text{Ni}} = 0.18 \pm 0.01 M_{\odot}$ $E_{\text{K}} = (2.4 \pm 0.9) \times 10^{52}$ erg	$\sim 10^7$	BB	$> 3 \times 10^{49}$	Nickel decay

highly spinning ν NS deserves deeper attention in the core collapse of the CO star.

Therefore, the ν NS might have evolved from a triaxial Jacobi-like ellipsoid into the axially symmetric Maclaurin spheroid by emission of gravitational waves, as anticipated in early models of pulsars (Ostriker & Gunn 1969; Ferrari & Ruffini 1969; Ruffini & Wheeler 1971), and theoretically verified by Chandrasekhar (1970); Miller (1974). The triaxial configuration lives for a short time, i.e., about less than a second, due to the copious emission of gravitational waves, before the GRB emission. The gravitational-wave emission could be, in principle, detected for sources located at distances closer than 100 Mpc (see Rueda et al. 2022a, for details). This appears to be the only emission of gravitational waves associated with the long GRB in the BdHN scenario: the core-collapse leading to the ν NS radiates poor gravitational waves ($\sim 10^{-7} M_{\odot} c^2 \sim 10^{47}$ erg; see Dimmelmeier et al. 2002; Fryer & New 2011). In addition, given the stringent limits on the ultrarelativistic jetted emission, both in the GeV radiation and in the X-ray afterglow, previous gravitational waves estimates (e.g. Leiderschneider & Piran 2021) do not apply (Rueda et al. 2022b).

10.2. QED radiation process in the UPE

At every expansion and transparency of the e^+e^- plasma, the energy radiated by the plasma is paid by the Kerr BH that reduces its mass and angular momentum by amounts ΔM and ΔJ , respectively (see Section 5 for details). The lower value of the BH spin leads to a lower value of the induced electric field, which implies

that a new self-expansion and transparency can occur with a lower e^+e^- plasma energy (Moradi et al. 2021c; Rastegarnia et al. 2022). The QED process and the approach to transparency are analogous, but the plasma parameters are different, which explains the hierarchical structure and similarity of the spectra in the time-resolved analysis of the UPE.

10.3. Classic electrodynamics radiation in the GeV emission

At the end of the UPE phase, the induced electric field is still sufficiently high to power the GeV emission of the GRB, which is emitted in the polar regions above and below the BH within an angle $\approx 60^\circ$ from the polar axis. The radiation power, timescale, and the energy stored in the electric field to accelerate the electrons confabulate to power luminosities of the order of 10^{51} erg s $^{-1}$ in the GeV domain for magnetic fields $B_0 \sim 10^{11}$ G (Ruffini et al. 2019c; Moradi et al. 2021b; Rueda et al. 2022b). The acceleration and radiation process occurs thanks to the magnetic dominance, $B^2 - E^2 > 0$, and the existence of regions where the component of the electric field parallel to the magnetic field is non-zero, i.e., $\mathbf{E} \cdot \mathbf{B} \neq 0$. As for the UPE, it is the rotational energy of the BH, the reservoir, that powers this radiation process. The extension of this approach to AGNs (e.g., M87*, see Moradi et al. 2021b).

10.4. Additional knowledge from the Physics frontier: the TeV emission

As we will show in the following sections, the SN has triggered not only the path to the new physical processes and understandings of phenomena in the BdHN but there is also a focus on the part of GRB radiation that is not yet theoretically understood and has only recently begun in earth band experiments: TeV radiation. In particular, what is most impressive is the presence of the TeV radiation in the prompt phase of BdHN I GRB 190114C (Ruffini et al. 2021) as well as in the afterglow of a BdHN I GRB 180720B (Rueda et al. 2022a; Rastegarnia et al. 2022), and in the afterglow of GRB 190829A (Wang et al. 2022b).

The first crucial information possibly contributing to the understanding of these processes is the fact that the energy flux of the TeV is 20%–60% of the energy flux of the afterglow. The second essential information is that in the case of BdHN II GRB 190829A, the emission occurs without a BH (Wang et al. 2022b). These two observations lead to privilege an energy emission of the TeV radiation linked to the synchrotron emission of the rapidly spinning ν NS. This fact has driven us to predict the TeV luminosity of GRB 221009A (Aimuratov et al. 2022b).

Finally, new perspectives emerge from the knowledge on the seven Episodes of BdHNe presented in this article for long GRBs, for the analysis of short GRBs previously studied, e.g., GRB 140619B (Ruffini et al. 2015), GRB 090510 (Ruffini et al. 2016a), GRB 081024B and GRB 140402A (Aimuratov et al. 2017).

11. CONCLUSIONS

A new era in physics and astrophysics started in 1996 when the Beppo SAX satellite promoted the extension of the observational techniques from the gamma-rays, the domain where GRBs were initially discovered, to the X-rays, optical, and radio observations. Further extensions to GeV, TeV, and VHE emissions observations were soon implemented. Three main discoveries were made possible at the time: a) the presence in long GRBs of an afterglow with long-lasting X-ray emission (Costa et al. 1997). As we here show, these afterglows have contributed significantly to the long GRB understanding; b) the cosmological nature of the GRBs, implying energies up to 10^{54} erg (Metzger et al. 1997); and c) the outstanding spatial and temporal coincidence between the Type Ic SN 1998bw, with optical emission of 10^{49} erg (Galama et al. 1998), and the long GRB 980425 of 10^{48} erg (Ruffini et al. 2007). This article is rooted in explaining this outstanding coincidence and illustrates, as well, the exponential growth of knowledge in physics and astrophysics made possible by an equally impressive growth of new technologies.

We have recalled in the Introduction the earlier description of long GRBs as originating from a single BH and an ultrarelativistic jet, the “collapsar” model. The lengthy and gradual evolution to a binary progenitor follows the pioneering work of Fryer et al. (1999). A further change of perspective happened with the introduction of the concept of induced gravitational collapse (IGC Rueda & Ruffini 2012). There the idea was advanced that BHs in long GRBs were not primordial but could be created by reaching the critical mass of an already existing accreting NS during the evolution of the binary progenitor. We have also recalled how motivated by a multiyear inquiry of long GRBs, and we finally proposed the BdHN model with a $\sim 10M_{\odot}$ CO core and $\sim 2M_{\odot}$ NS binary companion as progenitors for long GRBs. The CO core collapse triggers the GRB event.

We have also recalled how the BdHN approach has gained relevance because of the observed spatial and temporal coincidences of long GRBs with type Ic SNe. Also, the SNe Ic progenitors have been traditionally assumed, on the ground of a multi-year stellar evolution analysis, to be ultra-stripped binaries, composed indeed of very similar CO core -NS binaries. This fact has been assumed as a guiding factor in further developing our BdHN model, which naturally leads to comprehending the occurrence of the SN Ic in coincidence with a family of long GRBs, presented in this article.

Section 2 recalls that the BdHN model assumes that the gravitational collapse of the CO core necessarily leads to an SN with $7\text{--}8M_{\odot}$ ejecta and a millisecond spinning ν NS of $1.5M_{\odot}$, at its center. Both theoretical arguments and observational evidence for these assumptions are later justified in the article. Still in Section 2 we recall that ultra-stripped binaries comprise 0.1–1% of the total SNe, and that BdHNe represents only the 0.01–0.1% of the expected ultra-stripped binaries (see Fryer et al. 2015, and references therein).

This article addresses the identification of the separatrix properties of the CO core’s gravitational collapse occurring in binaries NS-CO core and leading, alternatively, to a single Ic SN or a similar SN Ic and a variety of long GRBs. It is shown that the most general BdHN, in addition to a standard Ic SN, leads to 1) an HN 10^3 times more energetic than a typical SN Ic, 2) to long GRBs, much more energetic than the SN Ic, in the range of $10^{49}\text{--}10^{54}$ erg 3) these long GRBs being subdivided in BdHN I, BdHN II, and BdHN III.

From observations and theoretical analysis, we illustrate in Section 2 the BdHN I with energies between 10^{52} erg and 10^{54} erg, the only BdHNe where a BH is formed by the IGC process, BdHN II with energies between 10^{50} erg and 10^{52} erg, and BdHN III with energies

below 10^{50} erg. For each BdHN type, we have identified the typical CO core-NS orbital period and the ν NS spin: the former ranges from ~ 4 –5 min in BdHN I, ~ 20 min in BdHN II, and to a few hours in BdHN III. Correspondingly, the ν NS spin ranges between 1 and 100 ms. A long-lasting X-ray afterglow is associated with *each* GRB and is present in *all* BdHN types. Specific examples are given in Section 6–9.

Already on these results, the important conclusion can be inferred that BdHNe are intrinsically dominated by a large amount of rotational energy; see text and references therein:

1. The ν NS spin inferred from the energetics of the X-ray afterglows has an initial dimensionless angular momentum $a/M = cJ/(GM^2)$, being J and M the ν NS angular momentum and mass, of ~ 0.5 for BdHN I down to $\sim 10^{-3}$ in BdHN III. We have given an example of how the fast spinning ν NS in GRB 180720B initially follows a Jacobi ellipsoid sequence (Rueda et al. 2022a), an absolute first in relativistic astrophysics.
2. The BH is formed only in BdHN I by the IGC process due to the accretion of SN ejecta onto the companion NS. Also, in this case, an initial dimensionless parameter ~ 0.5 of the BH has been inferred from the two BHs in BdHNI, GRB 180720B (see Section 6) and GRB 19014C (see Section 7).
3. As recalled above, the CO core gravitational collapse originates the entire energetics of the BdHN. Traditionally, the initial rotational energy of the CO core is assumed to be zero. Possibly the largest change of paradigm introduced by the BdHN model has been to point out that the zero angular momentum traditionally assumed in the description of the collapse of the CO core is untenable. In the BdHN model, the CO core has to be close to corotation with the binary NS companion: this implies, for a binary companion NS of ~ 4 min orbital period, a CO core with $a/m \sim 1$, assuming a radius $\sim 10^{10}$ cm and a mass $\sim 10M_\odot$. All efforts should be directed at gaining observational evidence for this corotation and developing an SN explosion model consistent with this assumption.

In Section 3, we have recalled relativistic transformations to evaluate the time measurement and the bolometric luminosities in the rest frame of the source. In Section 4, we present a selected sample of 24 spectroscopically confirmed SN Ic and their associated long GRBs (see Table 1). The main outcome is that all observed SNe Ic have peak luminosities around an average

value of 9.45×10^{42} erg s $^{-1}$ independently of the source redshift (see Fig. 2). The time of occurrence of the peak optical luminosity, measured from the GRB trigger, peaks at an average value of 1.16×10^6 s (see Fig. 3), again independently of the redshift of the source.

The properties of the associated GRBs for the selected three BdHNe classes are correspondingly summarized: 1) Figure 4 shows that the luminosity of the SN Ic has roughly the same value, BdHNe E_{iso} ranges from 10^{48} erg to 10^{54} erg. 2) Figure 5 shows that the time of occurrence of the peak luminosity of the SN Ic is also independent of the energetics of the associated BdHN. 3) The HN energy is 10^3 times larger than the common SN Ic. This decoupling between the GRBs and the Ic SN was highlighted in a pioneering work of Zeh et al. (2004) where this problem was announced, which we quantify and explain.

In Section 5, we indicate the BdHN approach in addressing using quantum and classical field theories, the conceptual description of a selected number of Episodes are then subjected to observational scrutiny via a time-resolved spectral analysis in the rest frame of the BdHN. The case is presented for the necessity of introducing and verifying new physical laws: either in extrapolating well-known physical laws already studied on Earth-bound experiments (see, e. g., Ruffini et al. 2010), now extended to new more extreme regimes encountered for the first time in extragalactic sources. This is the case of the classical electrodynamics processes extended to overcritical fields. Equally important has been to review the introduction of new physical laws in the quantum electrodynamics regimes to probe the process of rotational energy extraction from non-stationary and non-asymptotically flat Kerr solution as explaining the high energy GeV emission of GRBs. Particularly important has been the observational verification of the energy extraction process from a Kerr BH embedded in a fully ionized low-density plasma with a non-flat asymptotic solution given by a magnetic field aligned with the rotation axis of the Kerr solution. These new approaches, previously published in specific cases, are here directly applied in interpreting *all* seven Episodes of the most general BdHN, which are here briefly recalled while details are presented in Section 5.

Section 5.0: the SN-rise. We introduce, in this Episode, the first appearance of the CO core collapse and the SN explosion. This episode has been possibly observed in three BdHNe and needs further examples to verify its spectrum unambiguously. In this sense, we indicate this as Episode *zero*, waiting for the ongoing analysis of GRB 221009A, one of the most promising candidates. This Episode’s observation is particularly difficult

given its intrinsically low luminosity that in both BdHN I candidates precedes by a large time interval of ≈ 100 s, the ν -rise, and the UPE, the two first Episodes of the prompt radiation.

Section 5.1: the ν NS-rise. This Episode is identifiable by CPL spectra and its time of occurrence, manifesting the early presence of rapidly spinning ν NS. Their periods range from ~ 1 ms in BdHN I to ~ 100 ms in BdHN III. The ν NS-rise occurs in all BdHN types. It is further followed by the Synchrotron emission emitted by the ν NS interacting with the SN ejecta and leading to the three components afterglow: in the X-ray, in the optical and the radio, further examined in Section 5.5. One of the main results reached in the analysis of the ν NS-rise in the two BdHN I, GRB 180720B and GRB 190114C, has been the first observations of an initial tri-axial Jacobi ellipsoid evolving in a Maclaurin spheroid, with possible emission of gravitational waves. It is interesting that the presence of afterglows in *all* GRBs (observed in 380 BdHN I and all BdHN II and BdHN III) necessarily also implies the presence of ν NS in *all* GRBs.

Section 5.2: the UPE phase. The SN accretion onto the binary NS companion, soon after the first observation of the ν NS-rise, leads to the formation by the IGC process of a rapidly spinning Kerr BH whose presence is highlighted by the emission of the Ultra-relativistic Prompt Emission (UPE). In this section, we present an extended introduction of the theoretical works developed to extend to overcritical fields, i.e., $E \geq E_c = m_e^2 c^3 / (e\hbar) \approx 1.32 \times 10^{16}$ V cm $^{-1}$, to the multiyear theoretical works on vacuum polarization. This treatment is now finally reaching its observational verification in the GRBs. The overcritical field is due to an effective charge given by $Q_{\text{eff}} = 2B_0 JG/c^3$, being B_0 the magnetic field and J the angular momentum of the Kerr BH. These verifications on two selected BdHNe I, GRB 190114C, and GRB 180720B, have allowed explaining the existence of detailed new spectral features with the presence of self-similarities and structures on ever-decreasing time intervals to 10^{-9} s. The UPE phase has allowed to test observationally and verify the validity of the Christodoulou-Ruffini(Christodoulou & Ruffini 1971)-Hawking (Hawking 1971) mass-energy formula. This has allowed us to estimate the initial mass-energy of the Kerr BH and the associated magnetic field, B_0 , in both BdHNe I examined.

Section 5.3: High-energy jetted (GeV) emission. In this section, we study the high energy GeV emission originating from the classical electrodynamics process that transitions from the overcritical field, characterizing the UPE phase, to an undercritical field. The

theoretical analysis of the emission originated from a Kerr BH in the presence of a magnetic field of.. has allowed inferring an emission of the GeV radiation within a cone of half-opening of $\approx 60^\circ$ (Rueda et al. 2022b). This has been confirmed by the statistical analysis of the 54 BdHNe observed by Fermi-LAT. Only 25 emit the GeV radiation and the remaining 29, confirming not observable given the beamed radiation (Ruffini et al. 2021). Equally important has been the specific temporal power-law behavior of the GeV luminosity, well evidenced in Section 6 dedicated to GRB 180720B and Section 7 dedicated to GRB 190114C.

Section 5.4: The BH echoes. The cavity radiation, explained by the collision and partial reflection of the expanding e^+e^- with the cavity's wall, originated from the BH formation (Ruffini et al. 2019a), is evidenced for GRB 180720B in Section 6 and GRB 190114C in Section 7. The HXFs and SXFs, previously explained by the interaction of the expanding e^+e^- with the surrounding accretion matter, are observable in sources with observation angle in the equatorial plane of the BdHN (Ruffini et al. 2018g). These processes are identified in Section 6 for GRB 180720B. Neither HXF nor SXF is present in GRB 190114C, given the viewing angle orthogonal to the plane of orbit.

Section 5.5: Multiwavelength (X, optical, radio) afterglow. In this section, the afterglow's multi-wavelength X-ray, optical, and radio emissions are recalled with references to their theoretical treatments. We here recall that the afterglows are observed in *all* BdHN types, implying a large angle emission perfectly explained in terms of the synchrotron radiation emission process originating in a millisecond period of spinning ν NS as described in the following Sections 6 and 7. The afterglow is observed in *all* BdHNe, implying that all these GRBs originate from a CO-NS binary.

Section 5.6: The classic SN emission powered by nickel decay. In this section, we address the optical SN emission due to the nickel decay well expressed by the theoretical work of Nadyozhin (see, e.g., Nadyozhin's lectures, Nadyozhin 2011a,b) and Arnett (Arnett 1982). The crucial point is to recall that SN Ic is present in all BdHN types and observable with current telescopes for $z \lesssim 1$. New telescopes, e.g., the James Webb Space Telescope, should probe the presence of an SN, which is predicted to exist also for higher z values, following the BdHN model. We refer to Table 1 for a summary.

We turn then to the two examples of BdHNe I. In Section 6, we have summarized the results of GRB 180720B, and in Section 7 of GRB 190114C. In Section 8, we give the example of a BdHN II, GRB 190829A, and finally, in Section 9, the case of a BdHN III, GRB 171205A.

For each source, we have given: 1) the complete references to the observational papers we have utilized to perform the theoretical and the time-resolved spectral analysis; 2) a Figure summarising the luminosities for each Episode as a function of the rest-frame time and concerning the specific instruments and bandwidths. The same figure shows the specific examples of the spectra of each Episode; and 3) again, for each source, we present a Table summarizing the names of the observed Episodes: for each, we give the name of the event, the duration, the spectrum the corresponding E_{iso} and the underlying physical phenomena. A specific time-resolved spectral analysis of the UPE phase is exemplified in the case of GRB 190114C. In addition to the complete material for the description of two BdHN I, one BdHN II, and one BdHN III, we would like to mention that preliminary results have already been obtained for the UPE phase of two additional BdHN I, namely GRB 160626B and GRB 160509A (?). There, one can find the detailed UPE analysis for GRB 160625B in Table 2, Fig. 4, as well as Fig. 5, and for GRB 160509 in Table 4, Fig. 8, and Fig. 9. We are currently working on the identification of the other six Episodes present in both sources.

Following the above, we identify the primary energy source of all BdHN, independently of their type. The most remarkable property which has allowed us to understand the nature of GRBs has been the possibility to retrace back from the extraordinary observed spectral data, the specific energy sources, and their fundamental new physics. This has been made possible by the guidance of the BdHN model. We refer to the Figures and the Tables in the text and the references to the data acquisitions we have performed.

In Section 10, we briefly highlight the three main topics in which the analysis of the BdHN has promoted new research perspectives with the discovery of new physical laws and the verification of existing laws in new regimes made possible by the unique GRBs and HNe observations. The study of rotating figures of equilibrium represents one of the topics of research in which the best intellectuals have addressed their attention for over two centuries: from the self-gravitating Maclaurin spheroids to the discovery of the triaxial Jacobi ellipsoids. Now, for the first time, we have given evidence that triaxial ellipsoids can play a fundamental role in relativistic astrophysics and be the most prominent source of gravitational waves (Rueda et al. 2022a). Furthermore, far from being a conclusion, this is just the beginning of a new era in relativistic astrophysics leading to a new understanding of the physics of gravitational collapse of the creation of new physical systems by gravitational fission, to a new physics of SN explosion based on quan-

tum and classical electrodynamics process coupled to the rotational energy extraction.

Similarly, we have indicated the perspectives of classic and quantum electrodynamics energy extraction processes from rotating NS and Kerr BHs. The examples of the UPE phase and the GeV emission are here recalled just as interesting prototypes to be further extended. But far from being self-exhaustive, the GRB observations still present new challenges by the observations of vast amounts of TeV radiation up to luminosities of 10^{52} erg s $^{-1}$. At the same time, these emissions have recently been observed, in very low fluxes, in Earth-based accelerators, e.g., at CERN. Possibly, the most exciting new perspective is that there is evidence that this most energetic emission *does not* originate from a rotating BH, as already shown in this article.

It looks equally promising the interpretation of previous results on short GRBs using the knowledge acquired from the BdHN seven Episodes, e.g., in GRB 140619B (Ruffini et al. 2015), GRB 090510 (Ruffini et al. 2016a), GRB 081024B and GRB 140402A (Aimuratov et al. 2017).

Having said all the above, we can return to explain the enormous energetic difference between an SN Ic and the associated HN and long GRB through the occurrence of seven specific episodes in the most general BdHN leading to these concluding remarks:

1. The associated SN Ic bolometric energy of 10^{49} erg originates from the nuclear physics process leading to the decay of a common amount of a fraction of $0.2 M_{\odot}$ to $0.5 M_{\odot}$ of nickel (see e. g. Nadyozhin 2011a,b; Arnett 1982), remarkably similar in all BdHN sources. The same explanation regarding nuclear physics applies to explain the common time of occurrence of the SN peak emission, identified as soon as the relativistic corrections are implemented.
2. The HNe in BdHN have kinetic energies of 10^{52} erg originating from the kinetic energy of $7-8 M_{\odot}$ ejecta, expanding mildly-relativistically, observed in all BdHN types.
3. Both the above kinetic energy and the formation of a highly spinning millisecond ν NS at the SN center should find an explanation in a CO core-collapse, duly considering the contribution of the rotational energy, again observed in all BdHN types.

Turning now to the GRBs:

1. The X-ray, optical, and radio emission of the afterglow, present in all BdHN types, ranging from

a few 10^{52} erg in BdHN I (GRB 190114C) down to 10^{49} erg in BdHN III (GRB 171205A), are powered by the synchrotron emission originating from the rotational energy of the ν NS interacting with the SN ejecta. The ν NS initial rotation period is 1–100 ms.

2. The MeV and GeV emissions observed in the prompt radiation phase, present only in BdHN I, ranging 10^{52} – 10^{54} erg, are powered by quantum and classical electrodynamics process originating from the extractable rotational energy of a Kerr BH, embedded in a fully ionized low-density plasma. The Kerr solution is neither stationary nor asymptotically flat, but in the presence of a magnetic field, B_0 , aligned with its rotation axis and fulfilling the Christodoulou-Ruffini (Christodoulou & Ruffini 1971)-Hawking (Hawking 1971) mass-energy formula. For the latest developments, see Rueda and Ruffini (submitted).
3. Only the MeV emission in the prompt radiation of BdHN II, of $\sim 10^{52}$ erg (see Table 5), originates from the accretion of the SN ejecta into the slowing rotating binary NS companion.

We can then conclude, generally, that SNe Ic and their associated long GRBs originate from CO-NS binary progenitors.

We advance the hypothesis that most CO-NS binaries, with a binary period longer than a few hours, lead only to SN Ic, without any associated pulsar, GRB, or HN. This point can be easily tested observationally. A CO core, with an initial $a/M \sim 1$, endowed with an initial

magnetic field of $\sim 10^3$ G, and density of $\sim 10^4$ g cm $^{-3}$, can indeed lead, in the process of gravitational collapse, to a triaxial ellipsoid. The consequent fission, Roche lobe bifurcation, can lead to a fast spinning ν NS and a most powerful explosion. Like in the UPE phase, this process is expected to be driven by a quantum electrodynamical process originating from an overcritical “effective charge”. This overcritical field can complete the comprehension of the GRB-SN connection and lead to a new understanding of some of the current open issues. This will undoubtedly sign a good starting point for approaching the yet unsolved problem of the SN explosion, mainly examined in the absence of rotation. But this brings us to a different topic: the multi-century works on the rotating equilibrium configurations, as recalled above, developed by Elie Cartan, Bernhard Riemann, James Hopwood Jeans and summarized in a series of articles by Subrahmanyan Chandrasekhar (Chandrasekhar 1969), also in collaboration with Enrico Fermi (Chandrasekhar & Fermi 1953). These works are finally reaching the test of astrophysical observations in relativistic astrophysics, which is only partly the article’s topic today.

We are developing the BdHN model in a series of papers and are in continuous contact with many scientists and collaborators. Particularly important have been the discussions with Roy Patrick Kerr and with editors and referees of the journals: they have constructively contributed to finalizing the presentation of our research. To all of them goes our heartfelt thanks.

REFERENCES

- Abdalla, H., Adam, R., Aharonian, F., et al. 2019, *Nature*, 575, 464
- Aimuratov, Y., Ruffini, R., Muccino, M., et al. 2017, *ApJ*, 844, 83
- Aimuratov, Y., Becerra, L., Bianco, C. L., et al. 2021, *GRB Coordinates Network*, 31056, 1
- . 2022a, *GRB Coordinates Network*, 32780, 1
- . 2022b, *GRB Coordinates Network*, 32802, 1
- Ajello, M., Arimoto, M., Axelsson, M., et al. 2019, *ApJ*, 878, 52
- Amati, L. 2006, *MNRAS*, 372, 233
- Arnett, W. D. 1982, *ApJ*, 253, 785
- Ashall, C., Mazzali, P. A., Pian, E., et al. 2019, *MNRAS*, 487, 5824
- Barthelmy, S. D., Barbier, L. M., Cummings, J. R., et al. 2005, *SSRv*, 120, 143
- Barthelmy, S. D., Cummings, J. R., D’Elia, V., et al. 2017, *GRB Coordinates Network*, 22184, 1
- Becerra, L., Bianco, C. L., Fryer, C. L., Rueda, J. A., & Ruffini, R. 2016, *ApJ*, 833, 107
- Becerra, L., Cipolletta, F., Fryer, C. L., Rueda, J. A., & Ruffini, R. 2015, *ApJ*, 812, 100
- Becerra, L., Ellinger, C. L., Fryer, C. L., Rueda, J. A., & Ruffini, R. 2019, *ApJ*, 871, 14
- Becerra, L., Guzzo, M. M., Rossi-Torres, F., et al. 2018, *ApJ*, 852, 120
- Becerra, L. M., Moradi, R., Rueda, J. A., Ruffini, R., & Wang, Y. 2022, *PhRvD*, 106, 083002

- Becerra, L. M., Moradi, R., Rueda, J. A., Ruffini, R., & Wang, Y. 2022, *Phys. Rev. D*, 106, 083002.
<https://link.aps.org/doi/10.1103/PhysRevD.106.083002>
- Bellm, E. C., & Cenko, S. B. 2018, *GRB Coordinates Network*, 23041, 1
- Berger, E., Fox, D. B., Cucchiara, A., & Cenko, S. B. 2008, *GRB Coordinates Network*, 8335, 1
- Berger, E., Chornock, R., Holmes, T. R., et al. 2011, *ApJ*, 743, 204
- Bianco, C. L., Ruffini, R., & Xue, S.-S. 2001, *A&A*, 368, 377
- Bissaldi, E., & Racusin, J. L. 2018, *GRB Coordinates Network*, 22980, 1
- Bloom, J. S., Kulkarni, S. R., Price, P. A., et al. 2002, *ApJL*, 572, L45
- Bolmer, J., Greiner, J., & Chen, T. W. 2019, *GRB Coordinates Network*, 25651, 1
- Breit, G., & Wheeler, J. A. 1934, *Physical Review*, 46, 1087
- Bright, J. S., Horesh, A., van der Horst, A. J., et al. 2019, *MNRAS*, 486, 2721
- Bufano, F., Pian, E., Sollerman, J., et al. 2012, *ApJ*, 753, 67
- Burrows, D. N., Hill, J. E., Nousek, J. A., et al. 2005, *SSRv*, 120, 165
- Caito, L., Bernardini, M. G., Bianco, C. L., et al. 2009, *A&A*, 498, 501
- Cano, Z., Wang, S.-Q., Dai, Z.-G., & Wu, X.-F. 2017, *Advances in Astronomy*, 2017, 8929054
- Cano, Z., de Ugarte Postigo, A., Pozanenko, A., et al. 2014, *A&A*, 568, A19
- Cappellaro, E. 2022, *Nuovo Cimento Rivista Serie*, 45, 549
- Cavallo, G., & Rees, M. J. 1978, *MNRAS*, 183, 359
- Chandrasekhar, S. 1969, *Ellipsoidal figures of equilibrium* (Yale University Press)
- . 1970, *ApJ*, 161, 571
- Chandrasekhar, S., & Fermi, E. 1953, *ApJ*, 118, 116
- Cherry, M. L., Yoshida, A., Sakamoto, T., et al. 2018, *GRB Coordinates Network*, 23042, 1
- Cherubini, C., Geralico, A., Rueda, H. J. A., & Ruffini, R. 2009, *PhRvD*, 79, 124002
- Chincarini, G., Moretti, A., Romano, P., et al. 2007, *The Astrophysical Journal*, 671, 1903
- Christodoulou, D. 1970, *Physical Review Letters*, 25, 1596
- Christodoulou, D., & Ruffini, R. 1971, *PhRvD*, 4, 3552
- Cipolletta, F., Cherubini, C., Filippi, S., Rueda, J. A., & Ruffini, R. 2015, *PhRvD*, 92, 023007
- Costa, E., Frontera, F., Heise, J., et al. 1997, *Nature*, 387, 783
- Covino, S., & Fugazza, D. 2018, *GRB Coordinates Network*, 23021, 1
- Crouzet, N., & Malesani, D. B. 2018, *GRB Coordinates Network*, 22988, 1
- Cucchiara, A., & Fumagalli, M. 2013, *GRB Coordinates Network*, 14207, 1
- Cucchiara, A., & Perley, D. 2013, *GRB Coordinates Network*, 15144, 1
- de Ugarte Postigo, A., Izzo, L., Thoene, C. C., et al. 2019, *GRB Coordinates Network*, 25677, 1
- D’Elia, V., D’Ai, A., Lien, A. Y., & Sbarufatti, B. 2017, *GRB Coordinates Network*, 22177, 1
- D’Elia, V., Campana, S., D’Ai, A., et al. 2018, *A&A*, 619, A66
- D’Elia, V., D’Ai, A., Sbarufatti, B., et al. 2019, *GRB Coordinates Network*, 23706, 1
- Della Valle, M. 2011, *International Journal of Modern Physics D*, 20, 1745
- Della Valle, M., Malesani, D., Benetti, S., et al. 2004, in *American Institute of Physics Conference Series*, Vol. 727, *Gamma-Ray Bursts: 30 Years of Discovery*, ed. E. Fenimore & M. Galassi, 403–407
- Della Valle, M., Chincarini, G., Panagia, N., et al. 2006a, *Nature*, 444, 1050
- Della Valle, M., Malesani, D., Bloom, J. S., et al. 2006b, *ApJL*, 642, L103
- Dichiara, S., Bernardini, M. G., Burrows, D. N., et al. 2019, *GRB Coordinates Network*, 25552, 1
- Dimmelmeier, H., Font, J. A., & Müller, E. 2002, *A&A*, 393, 523
- Dirac, P. A. M. 1930, *Proceedings of the Cambridge Philosophical Society*, 26, 361
- Eichler, David, Livio, Mario, Piran, Tsvi, & Schramm, David N. 1989, *Nature* (ISSN 0028-0836), 340, 126
- Euler, H. 1936, *Annalen der Physik*, 418, 398
- Falcone, A. D., Morris, D., Racusin, J., et al. 2007, *The Astrophysical Journal*, 671, 1921
- Fermi GBM Team. 2019, *GRB Coordinates Network*, 25551, 1
- Ferrari, A., & Ruffini, R. 1969, *ApJL*, 158, L71
- Feynman, R. P. 1948, *Reviews of Modern Physics*, 20, 367
- . 1949a, *Physical Review*, 76, 749
- . 1949b, *Physical Review*, 76, 769
- Flores, H., Covino, S., Xu, D., et al. 2013, *GRB Coordinates Network*, 14491, 1
- Fox, D. W., Price, P. A., Soderberg, A. M., et al. 2003, *ApJL*, 586, L5
- Fraija, N., Dichiara, S., Pedreira, A. C. C. d. E. S., et al. 2019, *ApJ*, 885, 29
- Frederiks, D., Golenetskii, S., Aptekar, R., et al. 2016, *GRB Coordinates Network*, 20323, 1
- . 2017, *GRB Coordinates Network*, 22003, 1
- . 2018a, *GRB Coordinates Network*, 23061, 1
- . 2018b, *GRB Coordinates Network*, 23011, 1

- Fruchter, A. S., Levan, A. J., Strolger, L., et al. 2006, *Nature*, 441, 463
- Fryer, C. L., & New, K. C. B. 2011, *Living Reviews in Relativity*, 14, 1
- Fryer, C. L., Oliveira, F. G., Rueda, J. A., & Ruffini, R. 2015, *Physical Review Letters*, 115, 231102
- Fryer, C. L., Rueda, J. A., & Ruffini, R. 2014, *ApJL*, 793, L36
- Fryer, C. L., Woosley, S. E., & Hartmann, D. H. 1999, *The Astrophysical Journal*, 526, 152
- Fryer, C. L., Mazzali, P. A., Prochaska, J., et al. 2007, *PASP*, 119, 1211
- Fynbo, J. P. U., de Ugarte Postigo, A., D’Elia, V., Xu, D., & Malesani, D. 2012, *GRB Coordinates Network*, 13477, 1
- Galama, T. J., Vreeswijk, P. M., van Paradijs, J., et al. 1998, *Nature*, 395, 670
- Ghirlanda, G., Ghisellini, G., & Lazzati, D. 2004, *ApJ*, 616, 331
- Golenetskii, S., Aptekar, R., Frederiks, D., et al. 2013, *GRB Coordinates Network*, 14487, 1
- Goodman, J. 1986, *ApJL*, 308, L47
- Greiner, J., Mazzali, P. A., Kann, D. A., et al. 2015, *Nature*, 523, 189
- Gropp, J. D., Kennea, J. A., Klingler, N. J., et al. 2019, *GRB Coordinates Network*, 23688, 1
- Guetta, D., & Della Valle, M. 2007, *ApJL*, 657, L73
- Hamburg, R., Veres, P., Meegan, C., et al. 2019, *GRB Coordinates Network*, 23707, 1
- Hawking, S. W. 1971, *Physical Review Letters*, 26, 1344
- Heger, A., Fryer, C. L., Woosley, S. E., Langer, N., & Hartmann, D. H. 2003, *ApJ*, 591, 288
- Heintz, K. E., Fynbo, J. P. U., Jakobsson, P., et al. 2019, *GRB Coordinates Network*, 25563, 1
- Heisenberg, W., & Euler, H. 1936, *Zeitschrift für Physik*, 98, 714
- Hjorth, J., & Bloom, J. S. 2012, in “The Gamma-Ray Burst - Supernova Connection”, Chapter 9 in *Cambridge Astrophysics Series*, Vol. 51, “Gamma-Ray Bursts”, ed. C. Kouveliotou, R. A. M. J. Wijers, & S. Woosley (Cambridge University Press), 169–190
- Höflich, P., Wheeler, J. C., & Wang, L. 1998, *arXiv e-prints*, astro
- Hu, Y. D., Castro-Tirado, A. J., Kumar, A., et al. 2021, *A&A*, 646, A50
- Infante, L., Garnavich, P. M., Stanek, K. Z., & Wyrzykowski, L. 2001, *GRB Coordinates Network*, 1152, 1
- Itoh, R., Murata, K. L., Tachibana, Y., et al. 2018, *GRB Coordinates Network*, 22983, 1
- Iwamoto, K., Mazzali, P. A., & Nomoto, K. 1999, in *Japanese-German Workshop on High Energy Astrophysics*, ed. W. Becker & M. Itoh, 123
- Iwamoto, K., Nomoto, K., Höflich, P., et al. 1994, *ApJL*, 437, L115
- Izzo, L., Kann, D. A., de Ugarte Postigo, A., et al. 2018, *GRB Coordinates Network*, 23040, 1
- Izzo, L., Rueda, J. A., & Ruffini, R. 2012, *A&A*, 548, L5
- Izzo, L., Selsing, J., Japelj, J., et al. 2017, *GRB Coordinates Network*, 22180, 1
- Izzo, L., de Ugarte Postigo, A., Maeda, K., et al. 2019, *Nature*, 565, 324
- Jelinek, M., Strobl, J., Hudec, R., & Polasek, C. 2018, *GRB Coordinates Network*, 23024, 1
- Jordana-Mitjans, N., Mundell, C. G., Kobayashi, S., et al. 2020, *ApJ*, 892, 97
- Kankare, E., O’Neill, D., Izzo, L., et al. 2017, *GRB Coordinates Network*, 22002, 1
- Kann, D. A., Izzo, L., & Casanova, V. 2018, *GRB Coordinates Network*, 22985, 1
- Kann, D. A., Thoene, C. C., Selsing, J., et al. 2019, *GRB Coordinates Network*, 23710, 1
- Kelly, P. L., Kirshner, R. P., & Pahre, M. 2008, *ApJ*, 687, 1201
- Kennea, J. A., Sbarufatti, B., Burrows, D. N., et al. 2017, *GRB Coordinates Network*, 22183, 1
- Kim, H.-J., Yoon, S.-C., & Koo, B.-C. 2015, *ApJ*, 809, 131
- Klose, S., Schmidl, S., Kann, D. A., et al. 2019, *A&A*, 622, A138
- Kobulnicky, H. A., & Fryer, C. L. 2007, *ApJ*, 670, 747
- Kocevski, D., Omodei, N., Axelsson, M., et al. 2019, *GRB Coordinates Network*, 23709, 1
- Kohri, K., Narayan, R., & Piran, T. 2005, *ApJ*, 629, 341
- Kumar, A., Pandey, S. B., Gupta, R., et al. 2022, *NewA*, 97, 101889
- Leiderschneider, E., & Piran, T. 2021, *PhRvD*, 104, 104002
- Levan, A. J., Tanvir, N. R., Fruchter, A. S., et al. 2014, *ApJ*, 792, 115
- Li, L. 2022, *arXiv e-prints*, arXiv:2211.12187
- Lian, J.-S., Wang, S.-Q., Gan, W.-P., Li, J.-Y., & Liang, E.-W. 2022, *ApJ*, 931, 90
- Lien, A., Sakamoto, T., Barthelmy, S. D., et al. 2016, *ApJ*, 829, 7
- Lindner, C. C., Milosavljević, M., Shen, R., & Kumar, P. 2012, *ApJ*, 750, 163
- Lipunov, V., Gorboskoy, E., Tiurina, N., et al. 2018, *GRB Coordinates Network*, 23023, 1
- Lyman, J. D., Bersier, D., James, P. A., et al. 2016, *MNRAS*, 457, 328
- MacFadyen, A. I., & Woosley, S. E. 1999, *ApJ*, 524, 262

- Maeda, K., Nomoto, K., Mazzali, P. A., & Deng, J. 2006, *ApJ*, 640, 854
- MAGIC Collaboration, Acciari, V. A., Ansoldi, S., et al. 2019, *Nature*, 575, 455
- Maity, B., & Chandra, P. 2021, *ApJ*, 907, 60
- Mao, S., & Yi, I. 1994, *ApJL*, 424, L131
- Margutti, R., Guidorzi, C., Chincarini, G., et al. 2010, *Monthly Notices of the Royal Astronomical Society*, 406, 2149
- Martone, R., Guidorzi, C., Kobayashi, S., et al. 2018, *GRB Coordinates Network*, 22976, 1
- Mazzali, P. A., Deng, J., Tominaga, N., et al. 2003, *ApJL*, 599, L95
- Mazzali, P. A., Deng, J., Pian, E., et al. 2006, *ApJ*, 645, 1323
- Melandri, A., Izzo, L., D’Avanzo, P., et al. 2019, *GRB Coordinates Network*, 23983, 1
- Melandri, A., Izzo, L., Pian, E., et al. 2022, *A&A*, 659, A39
- Mészáros, P. 2002, *ARA&A*, 40, 137
- Meszáros, P., Laguna, P., & Rees, M. J. 1993, *ApJ*, 415, 181
- Mészáros, P., & Rees, M. J. 2001, *ApJL*, 556, L37
- Metzger, M. R., Djorgovski, S. G., Kulkarni, S. R., et al. 1997, *Nature*, 387, 878
- Miller, B. D. 1974, *ApJ*, 187, 609
- Milosavljević, M., Lindner, C. C., Shen, R., & Kumar, P. 2012, *ApJ*, 744, 103
- Minaev, P. Y., & Pozanenko, A. S. 2019, *Monthly Notices of the Royal Astronomical Society*, 492, 1919.
<https://doi.org/10.1093%2Fmnras%2Fstz3611>
- Mirzoyan, R., Noda, K., Moretti, E., et al. 2019, *GRB Coordinates Network*, 23701, 1
- Moradi, R., Li, L., Rueda, J. A., et al. 2021a, *arXiv e-prints*, arXiv:2103.09158
- Moradi, R., Rueda, J. A., Ruffini, R., & Wang, Y. 2021b, *A&A*, 649, A75
- Moradi, R., Rueda, J. A., Ruffini, R., et al. 2021c, *PhRvD*, 104, 063043
- Mulchaey, J., Kasliwal, M. M., Arcavi, I., Bellm, E., & Kelson, D. 2013, *The Astronomer’s Telegram*, 5191, 1
- Nadyozhin, D. K. 2011a, in *IRAP Ph.D. Erasmus Mundus Workshop - Les Houches - April 2011*,
<https://www.icranet.org/images/stories/Meetings/LES-HOUCHES/presentations/Nadyozhin1.pdf>
- Nadyozhin, D. K. 2011b, in *IRAP Ph.D. Erasmus Mundus Workshop - Les Houches - April 2011*,
<https://www.icranet.org/images/stories/Meetings/LES-HOUCHES/presentations/Nadyozhin2.pdf>
- Nakar, E., & Piran, T. 2017, *ApJ*, 834, 28
- Narayan, R., Paczynski, B., & Piran, T. 1992, *ApJL*, 395, L83
- Narayan, R., Piran, T., & Shemi, A. 1991, *ApJL*, 379, L17
- Negoro, H., Tanimoto, A., Nakajima, M., et al. 2018, *GRB Coordinates Network*, 22993, 1
- Nomoto, K., & Hashimoto, M. 1988, *PhR*, 163, 13
- Nomoto, K., Maeda, K., Nakamura, T., et al. 2003, in *Origin of Matter and Evolution of Galaxies 2000*, 223–239
- Ostriker, J. P., & Gunn, J. E. 1969, *ApJ*, 157, 1395
- Paczynski, B. 1986, *ApJL*, 308, L43
- Pandey, S. B., Anupama, G. C., Sagar, R., et al. 2003, *A&A*, 408, L21
- Patat, F., Cappellaro, E., Danziger, J., et al. 2001, *ApJ*, 555, 900
- Perley, D. A., & Cockeram, A. M. 2019a, *GRB Coordinates Network*, 25623, 1
- . 2019b, *GRB Coordinates Network*, 25657, 1
- Pian, E., Mazzali, P. A., Masetti, N., et al. 2006, *Nature*, 442, 1011
- Piran, T. 2004, *Reviews of Modern Physics*, 76, 1143
- Piran, T., Shemi, A., & Narayan, R. 1993, *MNRAS*, 263, 861
- Poolakkil, S., Preece, R., Fletcher, C., et al. 2021, *ApJ*, 913, 60
- Price, D. J. 2011, *SPLASH: An Interactive Visualization Tool for Smoothed Particle Hydrodynamics Simulations*, *Astrophysics Source Code Library*, ascl:1103.004
- Prochaska, J. X., Bloom, J. S., Chen, H. W., et al. 2003, *GRB Coordinates Network*, 2482, 1
- Ramirez-Ruiz, E., Celotti, A., & Rees, M. J. 2002, *MNRAS*, 337, 1349
- Raskin, C., Scannapieco, E., Rhoads, J., & Della Valle, M. 2008, *ApJ*, 689, 358
- Rastegarnia, F., Moradi, R., Rueda, J. A., et al. 2022, *European Physical Journal C*, 82, 778
- Rees, M. J., & Meszaros, P. 1992, *MNRAS*, 258, 41P
- Roberts, O. J., & Meegan, C. 2018, *GRB Coordinates Network*, 22981, 1
- Roming, P. W. A., Kennedy, T. E., Mason, K. O., et al. 2005, *SSRv*, 120, 95
- Ronchi, M., Fumagalli, F., Ravasio, M. E., et al. 2020, *A&A*, 636, A55
- Rossi, A., Izzo, L., Milvang-Jensen, B., et al. 2018, *GRB Coordinates Network*, 23055, 1
- Rueda, J. A. 2021, *Astronomy Reports*, 65, 1026
- Rueda, J. A., Li, L., Moradi, R., et al. 2022a, *ApJ*, 939, 62
- Rueda, J. A., & Ruffini, R. 2012, *ApJL*, 758, L7
- . 2020, *European Physical Journal C*, 80, 300
- Rueda, J. A., Ruffini, R., Karlica, M., Moradi, R., & Wang, Y. 2020, *ApJ*, 893, 148
- Rueda, J. A., Ruffini, R., & Kerr, R. P. 2022b, *ApJ*, 929, 56

- Rueda, J. A., Ruffini, R., Li, L., et al. 2022, *Phys. Rev. D*, 106, 083004.
<https://link.aps.org/doi/10.1103/PhysRevD.106.083004>
- Rueda, J. A., Ruffini, R., Li, L., et al. 2022a, *PhRvD*, 106, 083004
- . 2022b, *International Journal of Modern Physics D*, 31, 2230013
- Rueda, J. A., Ruffini, R., Moradi, R., & Wang, Y. 2021, *International Journal of Modern Physics D*, 30, 2130007
- Rueda, J. A., Ruffini, R., & Wang, Y. 2019a, *Universe*, 5, 110
- Rueda, J. A., Ruffini, R., Wang, Y., et al. 2018, *JCAP*, 10, 006
- . 2019b, *JCAP*, 2019, 044
- Ruffini, R., Karlica, M., Sahakyan, N., et al. 2018a, *ApJ*, 869, 101
- Ruffini, R., Melon Fuksman, J. D., & Vereshchagin, G. V. 2019a, *ApJ*, 883, 191
- Ruffini, R., Vereshchagin, G., & Xue, S. 2010, *PhR*, 487, 1
- Ruffini, R., & Wheeler, J. A. 1971, in *Proc. The Astrophysical Aspects of Weak Interactions*, 10–12 June 1970, *Problemi Attuali di Scienza e di Cultura* (Roma: Accademia Nazionale dei Lincei), 165–186
- Ruffini, R., Bernardini, M. G., Bianco, C. L., et al. 2007, in *ESA Special Publication*, Vol. SP-622, *The 6th Integral Workshop - The Obscured Universe*, ed. S. Grebenev, R. Sunyaev, C. Winkler, A. Parmar, & L. Ouwehand, 561
- Ruffini, R., Bianco, C. L., Enderli, M., et al. 2013, *GRB Coordinates Network*, 14526, 1
- Ruffini, R., Muccino, M., Kovacevic, M., et al. 2015, *ApJ*, 808, 190
- Ruffini, R., Muccino, M., Aimuratov, Y., et al. 2016a, *ApJ*, 831, 178
- Ruffini, R., Rueda, J. A., Muccino, M., et al. 2016b, *ApJ*, 832, 136
- Ruffini, R., Aimuratov, Y., Bianco, C. L., et al. 2018b, *GRB Coordinates Network*, 23019, 1
- Ruffini, R., Rodriguez, J., Muccino, M., et al. 2018c, *ApJ*, 859, 30
- Ruffini, R., Aimuratov, Y., Bianco, C. L., et al. 2018d, *GRB Coordinates Network*, 23066, 1
- Ruffini, R., Wang, Y., Aimuratov, Y., et al. 2018e, *ApJ*, 852, 53
- Ruffini, R., Aimuratov, Y., Bianco, C. L., et al. 2018f, *GRB Coordinates Network*, 23019, 1
- Ruffini, R., Becerra, L., Bianco, C. L., et al. 2018g, *ApJ*, 869, 151
- Ruffini, R., Moradi, R., Aimuratov, Y., et al. 2019b, *GRB Coordinates Network*, 23715, 1
- Ruffini, R., Moradi, R., Rueda, J. A., et al. 2019c, *ApJ*, 886, 82
- Ruffini, R., Li, L., Moradi, R., et al. 2019d, *arXiv e-prints*, arXiv:1904.04162
- Ruffini, R., Moradi, R., Rueda, J. A., et al. 2021, *MNRAS*, 504, 5301
- Sana, H., de Mink, S. E., de Koter, A., et al. 2012, *Science*, 337, 444
- Sasada, M., Nakaoka, T., Kawabata, M., et al. 2018, *GRB Coordinates Network*, 22977, 1
- Sauter, F. 1931a, *Zeitschrift fur Physik*, 69, 742
- . 1931b, *Zeitschrift fur Physik*, 73, 547
- Schmalz, S., Graziani, F., Pozanenko, A., et al. 2018, *GRB Coordinates Network*, 23020, 1
- Schulze, S., Malesani, D., Cucchiara, A., et al. 2014, *A&A*, 566, A102
- Schwinger, J. 1948, *Physical Review*, 74, 1439
- . 1949a, *Physical Review*, 75, 651
- . 1949b, *Physical Review*, 76, 790
- Selsing, J., Fynbo, J. P. U., Heintz, K. E., & Watson, D. 2019, *GRB Coordinates Network*, 23695, 1
- Sfaradi, I., Bright, J., Horesh, A., et al. 2018, *GRB Coordinates Network*, 23037, 1
- Shemi, A., & Piran, T. 1990, *ApJL*, 365, L55
- Siegel, M. H., Burrows, D. N., Deich, A., et al. 2018, *GRB Coordinates Network*, 22973, 1
- Smartt, S. J. 2009, *ARA&A*, 47, 63
- . 2015, *PASA*, 32, e016
- Smith, N., Li, W., Silverman, J. M., Ganeshalingam, M., & Filippenko, A. V. 2011, *MNRAS*, 415, 773
- Sparre, M., Sollerman, J., Fynbo, J. P. U., et al. 2011, *ApJL*, 735, L24
- Tanaka, M., Yamanaka, M., Maeda, K., et al. 2009, *ApJ*, 700, 1680
- Tanvir, N. R., Kruehler, T., Wiersema, K., et al. 2016, *GRB Coordinates Network*, 20321, 1
- Tauris, T. M., Langer, N., & Podsiadlowski, P. 2015, *MNRAS*, 451, 2123
- Teffs, J., Ertl, T., Mazzali, P., Hachinger, S., & Janka, T. 2020, *MNRAS*, 492, 4369
- Thöne, C. C., Greiner, J., Savaglio, S., & Jihin, E. 2007, *ApJ*, 671, 628
- Tsvetkova, A., Golenetskii, S., Aptekar, R., et al. 2019, *GRB Coordinates Network*, 25660, 1
- Ulanov, M. V., Golenetskii, S. V., Frederiks, D. D., et al. 2005, *Nuovo Cimento C Geophysics Space Physics C*, 28, 351
- Valeev, A. F., Castro-Tirado, A. J., Hu, Y. D., et al. 2019, *GRB Coordinates Network*, 25565, 1

- Vergani, S. D., Flores, H., Covino, S., et al. 2011, *A&A*, 535, A127
- Vreeswijk, P., Fruchter, A., Hjorth, J., & Kouveliotou, C. 2003, *GRB Coordinates Network*, 1785, 1
- Vreeswijk, P., Fynbo, J., & Melandri, A. 2011, *GRB Coordinates Network*, 12648, 1
- Vreeswijk, P. M., Kann, D. A., Heintz, K. E., et al. 2018, *GRB Coordinates Network*, 22996, 1
- Vurm, I., Hascoët, R., & Beloborodov, A. M. 2014, *ApJL*, 789, L37
- Wang, Y., Becerra, L. M., Fryer, C. L., Rueda, J. A., & Ruffini, R. 2022a, *arXiv e-prints*, arXiv:2208.02725
- Wang, Y., Rueda, J. A., Ruffini, R., et al. 2019, *ApJ*, 874, 39
- . 2022b, *ApJ*, 936, 190
- Watson, A. M., Butler, N., Becerra, R. L., et al. 2018, *GRB Coordinates Network*, 23017, 1
- Woosley, S. E. 1993, *ApJ*, 405, 273
- Woosley, S. E., & Bloom, J. S. 2006, *ARA&A*, 44, 507
- Xu, D., Yu, B. Y., Zhu, Z. P., & et al. 2019, *GRB Coordinates Network*, 25555, 1
- Yamazaki, R., Yonetoku, D., & Nakamura, T. 2003, *ApJL*, 594, L79
- Yoon, S.-C. 2015, *PASA*, 32, e015
- Yoon, S.-C., Woosley, S. E., & Langer, N. 2010, *ApJ*, 725, 940
- Zeh, A., Klose, S., & Hartmann, D. H. 2004, *ApJ*, 609, 952
- Zhang, B. 2018, *The Physics of Gamma-Ray Bursts* (Cambridge Univeristy Press), doi:10.1017/9781139226530
- . 2019, *Nature*, 575, 448
- Zhang, W., Woosley, S. E., & Heger, A. 2004, *ApJ*, 608, 365
- Zheng, W., & Filippenko, A. V. 2018, *GRB Coordinates Network*, 23033, 1